Geobiology of a Lower Cambrian Carbonate Platform, Pedroche Formation, Ossa Morena Zone, Spain

Keywords: Cambrian; carbonate; thrombolite; skeletons; archaeocyath

GEOBIOLOGY OF A LOWER CAMBRIAN CARBONATE PLATFORM, PEDROCHE FORMATION, OSSA MORENA ZONE, SPAIN

Jessica R. Creveling[a*1], David Fernández Remolar[b], Marta Rodríguez-Martínez[c], Silvia Menéndez[d], Kristin D. Bergmann[e], Benjamin C. Gill[f], John Abelson[g], Ricardo Amils[b,h], Bethany L. Ehlmann[e], Diego C. García-Bellido[i], John P. Grotzinger[e], Christian Hallmann[j,k], Kathryn M. Stack[e], Andrew H. Knoll[a,l]

[a]*Department of Earth and Planetary Sciences, Harvard University, Cambridge, MA, U.S.A., 02138*

[b]*Centro de Astrobiología (INTA-CSIC), INTA Campus, 28850 Torrejón de Ardoz, Spain*

[c]*Departamento de Estratigrafía, Facultad de Ciencias Geológicas, Universidad Complutense de Madrid, 28041 Madrid, Spain*

[d]*Museo Geominero, Instituto Geológico y Minero, 28003 Madrid, Spain*

[e]*Division of Geological and Planetary Sciences, California Institute of Technology, CA, U.S.A., 91125*

[f]*Department of Geosciences, Virginia Polytechnic Institute and State University, Blacksburg, VA, U.S.A. 24061*

[g]*The Agouron Institute, Pasadena, CA, U.S.A., 91106*

[h]*Centro de Biología Molecular Severo Ochoa, Universidad Autónoma de Madrid, 28048 Madrid, Spain*

[i]*Sprigg Geobiology Centre, School of Earth & Environmental Sciences, University of Adelaide, SA 5000, Adelaide, Australia*

[j]*Max-Planck-Institute for Biogeochemistry, 07745 Jena, Germany*

[k]*MARUM, Universität Bremen, 28359 Bremen, Germany*

[l]*Department of Organismic and Evolutionary Biology, Harvard University, Cambridge, MA, U.S.A., 02138*

*Corresponding author. E-mail address: jcrevel@gps.caltech.edu (J.R. Creveling). Tel.: +1 626 395 1783.

[1]Present address: California Institute of Technology, Division of Geological and Planetary Sciences, MC 100-23, 1200 E. California Blvd., Pasadena, CA, 91125, U.S.A.

ABSTRACT

The Cambrian Pedroche Formation comprises a mixed siliciclastic–carbonate succession recording subtidal deposition on a marine platform. Carbonate carbon isotope chemostratigraphy confirms previous biostratigraphic assignment of the Pedroche Formation to the Atdabanian regional stage of Siberia, correlative to Cambrian Series 2. At the outcrop scale, thrombolitic facies comprise ~60% of carbonate-normalized stratigraphy and coated-grains another ~10%. Petrographic point counts reveal that skeletons contribute at most 20% to thrombolitic inter-reef and reef-flank lithologies; on average, archaeocyath clasts make up 68% of skeletal materials. In contrast, petrographic point counts show that skeletons comprise a negligible volume of biohermal and biostromal thrombolite, associated nodular carbonate facies, and ooid, oncoid and peloid grainstone facies. As such, archaeocyathan reefal bioconstructions represent a specific and limited locus of skeletal carbonate production and deposition. Consistent with data from coeval, globally dispersed lower Cambrian successions, our analysis of the Pedroche Formation supports the view that early Cambrian carbonates have more in common with earlier, Neoproterozoic deposits than with younger carbonates dominated by skeletal production and accumulation.

1. INTRODUCTION

Today, skeletons account for most carbonate accumulation in the oceans (e.g., Sarmiento and Gruber, 2006). The geological record, however, shows that this was not the case for most of Earth history; Archean and Proterozoic successions contain thick packages of shallow-marine carbonates deposited via abiotic and microbially-mediated precipitation (e.g., Grotzinger, 1989; Knoll and Swett, 1990; Grotzinger and James, 2000). With this in mind, a canonical view holds that the Cambrian diversification of skeletal animals (Maloof et al., 2010a; Kouchinsky et al., 2012) was a watershed event in the evolution of platform and shelf carbonate deposition (e.g., Zeebe and Westbroek, 2003). Yet, the idea that the nature of carbonate production irrevocably changed with the advent of skeletal biomineralization is hard to reconcile with uppermost Neoproterozoic and Cambrian carbonates whose textures resemble Proterozoic platform archetypes despite a quantifiable skeletal contribution.

Where, then, do Cambrian shelf and platform carbonates fall along the spectrum of non-skeletal to skeletal control? Might the Cambrian Period represent a time when organisms had evolved biomineralized skeletons but not yet transformed the marine carbonate cycle? Analysis of upper Cambrian and lower Ordovician carbonates from Laurentia provides support for this view; in successions from Newfoundland and the North American Cordillera, skeletal material rarely exceeds 25% of bulk carbonate volume and is commonly much less (Pruss et al., 2010). Upper Cambrian rocks, however, might understate the case for skeletal input to Cambrian carbonates, in large part because archaeocyaths, the most conspicuous Cambrian reef-constructing animals, had nearly disappeared by 510 Ma (Debrenne, 2007). Preliminary research on earlier Cambrian carbonates suggests that skeletons contributed up to ~ 20% of total carbonate production, with archaeocyathan material dominating skeletal input (Hicks and

70 Rowland, 2009; Pruss et al., 2012).

71 Here we provide a new case study of carbonate production on an early Cambrian
72 carbonate platform that hosted archaeocyath-bearing thrombolite reefs. We focus on the nature
73 of carbonate production and the percent skeletal abundance within three stratigraphic sections of
74 the Cambrian Series 2 Pedroche Formation located near Córdoba, southern Spain, and build on a
75 sedimentological and biostratigraphic framework developed by numerous authors. The Pedroche
76 Formation at the Arroyo Pedroche section has been analyzed and discussed previously by
77 Carbonell (1926, 1929, 1930a-g), Cabanás and Meléndez (1966), Perejón (1975 a,b,c; 1976a,b;
78 1977, 1986, 1989), Cabanás (1971), Liñán (1974, 1978), Liñán and Dabrio (1974), Liñán et al.
79 (1981), Liñán and Mergl (1982), Schmitt (1982), Moreno-Eiris (1987 a,b,c,d), Moreno-Eiris et
80 al. (1995), and Fernández-Remolar (1996, 1998). The Pedroche Formation at the Cerro de Las
81 Ermitas section has been studied previously by Hernández Pacheco (1907; 1917; 1918a,b; 1926),
82 Hernández-Sampelayo (1933, 1935), Simon (1939), Perejón (1976a,b; 1971; 1975 a,b,c; 1986),
83 Cabanás (1971), Zamarreño and Debrenne (1977), Moreno-Eiris (1987 a,b,c,d), Fernández-
84 Remolar (1996, 1998, 1999, 2001, 2002), and Perejón and Moreno-Eiris (2007). Zamarreño
85 (1977) studied the Pedroche Formation at the Pilgrimage Road section.

86 To complement and extend this body of research, we use $\delta^{13}C_{carb}$ chemostratigraphy to
87 establish local and global temporal correlations. Next, we analyze the architecture of thrombolite
88 and associated carbonate facies from this mixed carbonate-siliciclastic platform developed on a
89 peri-Gondwana terrane during the early Cambrian. To do so, we follow the methodology of
90 Pruss et al. (2010) and use nested scale observations, from outcrop stratigraphy to petrographic
91 analysis of carbonate facies, to quantify the contribution of skeletal material to carbonate
92 lithofacies and assess the nature of carbonate production across the platform. Finally, we

93 compare these findings with other early Cambrian localities with quantitative lithologic and
94 skeletal composition data.
95
96 **2. GEOLOGIC SETTING**
97
98 The three outcrops of the Pedroche Formation studied here occur within the Sierra de Córdoba,
99 near the city of Córdoba, within the Ossa-Morena tectonostratigraphic zone of the Iberian Massif
100 (Fig. 1a)(Lotze, 1945; Julivert et al., 1972; Dallmeyer and Martínez García, 1990; Ábalos et al.,
101 2002; Pérez-Estaún and Bea, 2004). The Ossa-Morena zone records a complex history of
102 Neoproterozoic and Paleozoic extension, sedimentation and orogenesis resulting from the
103 geodynamic interactions among Gondwana, Laurentia, Baltica and proximal micro-continents,
104 including Iberia (see, for example, Eguíluz et al., 2000; Dallmeyer and Martínez García, 1990).
105 Broadly, the tectonostratigraphy of the Ossa-Morena zone documents Neoproterozoic Cadomian
106 and middle-to-late Paleozoic Hercynian orogenesis, each followed by sedimentation during rift-
107 to-drift (passive margin) transition (Eguíluz et al., 2000). These Neoproterozoic to Paleozoic
108 strata were uplifted in the southwest European Variscan Orogen as a result of collision between
109 Laurentia and Gondwana during the Devonian to Permian periods (Bard et al., 1980; Matte,
110 1991).
111 Liñán (1974, 1978) developed the Cambrian lithostratigraphic framework for the Sierra
112 de Córdoba region (Fig. 1b). Cambrian strata unconformably overlie the San Jerónimo
113 Formation of the Neoproterozoic volcanic-sedimentary complex (Liñán and Palacios, 1983;
114 Fedonkin et al., 1983). From oldest to youngest, the Cambrian stratigraphy is divided into the
115 following formations (see the overview in Gozalo et al., 2003): (i) the siliciclastic-dominated

Torreárboles Formation (0-300 m), assigned to the Spanish Corduban stage based on its trace fossil assemblage (Fedonkin et al., 1983); (ii) the mixed carbonate-siliciclastic Pedroche Formation (350 m), which represents the Ovetian stage (biostratigraphic references are discussed below); (iii) the mixed carbonate and siliciclastic Santo Domingo Formation (200 m) representing the Marianian stage; (iv) the Castellar Formation (~75 m), assigned to the Bilbilian stage based on stratigraphic position (Liñán et al., 1997); and (v) the siliciclastic Los Villares Formation (> 450 m) ranging from Bilbilian to middle Cambrian in age (Liñán and Sdzuy, 1978; Liñán 1978). Here we focus on the fossiliferous carbonates of the Pedroche Formation.

The Pedroche Formation records the first stable carbonate platform development after Cadomian rifting (Liñán and Quesada, 1990; Quesada, 1990; Menéndez et al., 1999). Trilobite (Liñán et al., 2005; Liñán et al., 2008), archaeocyath (Perejón, 1986; 1989; 1994) and small shelly fossil (SSF; Fernández-Remolar, 2001; Gubanov et al., 2004; Hinz-Schallreuter et al., 2008) biostratigraphy assign the Pedroche to the early Ovetian Stage of the Iberian chronostratigraphic framework (Liñán et al., 1993 and references therein). Archaeocyathan taxa of the Pedroche Formation correlate to Spanish archaeocyathan Zones I – III, correlative to the Atdabanian 1–2 stage of Siberia (Perejón and Moreno-Eiris, 2006). The occurrence of the bigotinid trilobites *Bigotina* and *Lemdadella* within these zones also supports an early Atdabanian age (Liñán and Gámez Vintanez, 1993; Liñán et al., 1995, 2005, 2008). As such, the Pedroche Formation records deposition correlative to Cambrian Series 2, Stage 3 of the international chronostratigraphy for the Cambrian System (Fig. 1b; Jensen et al., 2010; Babcock and Peng, 2007; Peng and Babcock, 2011).

3. METHODS

Stratigraphic sections of the Pedroche Formation were described and measured at three localities in the vicinity of Córdoba, Andalucía, Spain (Fig. 1a). The type section for the formation, at Arroyo Pedroche (Section AP; 37°54'26.67"N, 4°45'29.07"W), crops out along the east embankment of an arroyo. Additionally, the Pedroche Formation is exposed north-northeast of the city within the Sierra de Córdoba, where strata crop out along the north side of a hairpin turn on CO-110, herein referred to as Pilgrimage Road (Section PR; 37°55'45"N, 4°49'02"W), as well as on the east side of road CV-079 leading to Cerro de Las Ermitas (Section LE; 37°55'05.25"N, 4°49'34.66"W), just above the fifth station of the cross.

We determined the percent of carbonate lithofacies within each stratigraphic section by adding up the bed thicknesses of a lithofacies (e.g., ooid/oncoid/peloid grainstone), dividing this value by the total meterage from each section, and multiplying this decimal by 100 (Table 1). Likewise, we determined the 'carbonate-normalized' percent contribution of a carbonate lithofacies to a stratigraphic section through the method described above, except in this case we divide by the total carbonate meterage of the section. Within the lithofacies descriptions we use the terminology of Ingram (1954) to generalize laminae and bed thickness (thinly laminated: < 3mm; thickly laminated: 3–10 mm; very thinly bedded: 1–3 cm; thinly bedded: 3–10 cm; medium bedded: 10–30 cm; thickly bedded: 30–100 cm; and very thickly bedded: > 1m). Our field descriptions include cm-scale measurements of each bed in order to best estimate the percent contribution of each lithofacies to the three stratigraphic sections measured.

We collected hand samples of carbonate lithofacies at ~1 to 2 meter resolution. The samples were cut with a water-cooled saw perpendicular to bedding to create slabs and thin-section billets. Each slab or billet was micro-drilled with a 1 mm dental bit for carbonate carbon

($\delta^{13}C_{carb}$) and carbonate oxygen ($\delta^{18}O_{carb}$) isotopic analysis. We targeted micritic textures and avoided veins, cements and skeletal elements. Carbonate powder was reacted in a common phosphoric acid bath at 90°C for 7 minutes. Evolved CO_2 was cryogenically concentrated and measured against an in-house reference gas on a VG Optima dual-inlet mass spectrometer attached to a VG Isocarb preparation system. All isotopic values are reported in per mil (‰) notation relative to the V-PDB standard with a reproducibility of $1\sigma \approx 0.1$‰ and 0.3‰ for $\delta^{13}C_{carb}$ and $\delta^{18}O_{carb}$, respectively.

Point-counts of petrographic thin-sections enabled us to quantify the proportional contributions of constituent components to the total carbonate volume (e.g., Flügel, 2004; Payne et al., 2006; Pruss et al., 2010; Pruss and Clemente, 2011). Of the 74 thin-sections examined for lithofacies description, we point counted 30 thin sections for quantitative analysis of constituent components, with 5 representing the calcimicrobial thrombolite facies (facies A), 9 representing the ooid/oncoid/peloid grainstone facies (facies C), and 16 representing the interbedded carbonate mudstone, bioclastic wackestone, archaeocyathan floatstone–packstone–rudstone and siliciclastic siltstone facies assemblage (facies D; see Section 5 for lithofacies description; Table 2). We chose these thin sections because they exhibit the least secondary recrystallization (spar and veins) of all the hand samples collected.

The statistical robustness of point count frequency analyses depends on the density of the point array (grid spacing) with respect to the size and percent contribution of individual components (Van der Plas and Tobi, 1965; Flügel, 2004). Generally, the width of the chosen grid spacing relative to the largest diameter of the constituent components (e.g., micrite, ooids or archaeocyaths) dictates whether the counting procedure over-represents coarse grains (dense grid) or under-represents fine grains (sparse grid) (Van der Plas and Tobi, 1965; Flügel, 2004).

185 We used transmitted light microscopy to classify ~200 points per thin-section, corresponding to a
186 2 x 2 mm width grid spacing. This point-density translates to 2σ errors of ~2, 4, and 5.5% for
187 constituent components calculated to comprise ~3, 9, and 20% of the sample, respectively. In
188 other words, a sample determined to have 9% skeletal content by point-count analysis should be
189 considered to have 9 ± 4% with 95% confidence (Van der Plas and Tobi, 1965; Flügel, 2004).
190 Lithologies and microtextures of the Pedroche Formation, particularly the archaeocyath-
191 bearing facies, consist of submicron- to centimeter-scale crystals and grains. As such, the use of
192 a fixed grid spacing introduces a potential bias towards grains larger than 2 x 2 mm width /
193 circumference. We note, however, that the true skeletal component of large skeletal grains, such
194 as archaeocyaths, comprise only a fraction of the total encompassing volume. For this reason, we
195 employ the grain-solid method of point counting wherein only the solid fraction of a skeleton is
196 classified as skeletal contribution; any primary inter-skeletal void space, such as the central
197 cavity of an archaeocyath, is counted separately under relevant textural classifications, such as
198 micrite or sparry cement (Flügel, 2004). As such, we believe the chosen grid spacing should not
199 over represent the largest diameter constituents. We adopted this method from Pruss et al. (2012)
200 so that we could directly compare the percentage of constituent carbonate fabrics and, in
201 particular, the skeletal content of the Pedroche Formation to archaeocyath-bearing Cambrian
202 Series 2 reefs from the Forteau Formation, southern Labrador.
203 A subset of the thin-sections analyzed had surface areas too small to count 200 points per
204 slide at 2 mm spacing. Instead of increasing the point density (decreasing the grid spacing)
205 counted on these slides—which would have shifted the bias in grain size relative to the 2 mm
206 grid—we report fewer than 200 points for these samples with the caveat that larger 2σ
207 uncertainties in the percent determinations of constituent components are associated with these

208 samples. Nevertheless, for this subset of samples we counted between 164 and 198 points,
209 therefore the additional uncertainly incurred from these lower point counts should not
210 significantly influence the conclusions of this study.
211
212 **4. CARBON ISOTOPIC CHEMOSTRATIGRAPHY**
213
214 Figure 2 presents a 3-point moving average of carbonate carbon isotope ($\delta^{13}C_{carb}$)
215 chemostratigraphy for the AP and PR sections, and un-averaged data for the LE section. (See
216 Supplementary Information for a table of raw $\delta^{13}C_{carb}$ and $\delta^{18}O_{carb}$ values, covariance plots of
217 $\delta^{13}C_{carb}$ versus $\delta^{18}O_{carb}$, and chemostratigraphic plots of both un-averaged and 3-point running
218 means of $\delta^{13}C_{carb}$ for all three stratigraphic sections.) Arroyo Pedroche $\delta^{13}C_{carb}$ values display a
219 positive trend from 1.9 to 3.3‰ from 32–37 m that precedes a negative excursion to a nadir of -
220 1.3‰ at 67 m. Above the covered interval from ~68.1–81 m, $\delta^{13}C_{carb}$ values resume at -2.0‰,
221 plateau at ~ -1.4‰ between 82.9–119.1 m, and increase to -0.5‰ by 129 m. At the Pilgrimage
222 Road section, $\delta^{13}C_{carb}$ values show a broadly similar pattern of stratigraphic variation, increasing
223 from -1.8 to 1.0‰ from the base of the section to 30.5 m, declining to a nadir of -2.9‰ at 52 m,
224 and then rebounding toward broadly stable values of -1 to -2 in the upper part of the section
225 (except for a transient negative excursion to -2.9‰ at 89 m). The carbon isotope composition of
226 carbonates of the Las Ermitas section remains invariant at ~ -1.5‰.
227 Correlation between $\delta^{13}C_{carb}$ and $\delta^{18}O_{carb}$ values in samples from the Arroyo Pedroche
228 section (0–63 m) and Las Ermitas section (0–13 m) is best explained by a linear regression
229 model ($R^2 = 0.71$ for both sections). Conversely, no linear covariance between $\delta^{13}C_{carb}$ and
230 $\delta^{18}O_{carb}$ values is observed in these two sections above these stratigraphic intervals ($R^2 = 0.15$

and 0.35, respectively), nor is covariance observed within the Pilgrimage Road section (R^2 = 0.14). Covariance between $\delta^{13}C_{carb}$ and $\delta^{18}O_{carb}$ values, as well as isotopically depleted $\delta^{18}O_{carb}$ values, provides strong evidence for diagenetic overprint of primary seawater isotopic compositions (e.g., Knauth and Kennedy, 2009; Derry, 2010 and references therein). While petrography indicates significant neomorphism of these limestones (see Section 5), petrographic textures do not differ between intervals with and without $\delta^{13}C_{carb}$–$\delta^{18}O_{carb}$ covariation.

An alternative way to address the possibility of whole rock diagenesis is to ask how well the chemostratigraphic variation within the Pedroche Formation correlates to chemostratigraphic variability from biostratigraphically equivalent time periods elsewhere around the globe. The well-constrained biostratigraphic assignment of Pedroche carbonates to the early Ovetian, equivalent to the base of Cambrian Series 2 and the Siberian Atdabanian Stage (Jensen et al., 2010) makes a prediction for their C-isotopic composition. Consistent with this prediction, $\delta^{13}C_{carb}$ values from Arroyo Pedroche appear to capture the apex of a positive excursion, with absolute values like those of the early Atdabanian Stage IV excursion in Siberia (Brasier et al., 1994; Kouchinsky et al., 2007). Within the Arroyo Pedroche section, these positive $\delta^{13}C_{carb}$ values precede a plateau of -1.5‰, further consistent with values recorded from expanded sections of early Atdabanian age (Maloof et al., 2005; Kouchinsky et al., 2007). Thus, chemostratigraphy corroborates biostratigraphic assignment of the Pedroche Formation to the lower part of Cambrian Series 2, Stage 3. Moreover, correlation of the Pedroche $\delta^{13}C_{carb}$ values to a radiometrically calibrated Cambrian Terreneuvian–Series 2 $\delta^{13}C_{carb}$ curve suggests an absolute depositional age between 520.93 ± 0.14 Ma and 517.0 ± 1.5 Ma (Maloof et al., 2010b; Landing et al., 1998).

253 If interpreted as faithful recorders of the isotopic composition of contemporaneous
254 seawater, the architecture and magnitude of $\delta^{13}C_{carb}$ variation within the three measured
255 stratigraphic sections suggests they record overlapping but not entirely equivalent time intervals
256 (Fig. 2). Specifically, isotopes imply that deposition of the Las Ermitas section correlates only
257 with the upper half of the succession at Arroyo Pedroche. Detailed correlation with the
258 Pilgrimage Road section is less clear. Many of the carbon isotopic values reported from
259 Pilgrimage Road are more negative and display more point-to-point variability than those
260 reported from either the Arroyo Pedroche or Las Ermitas sections. Carbonates at Pilgrimage
261 Road are often nodular, massively recrystallized, and/or interbedded with siliciclastic strata;
262 these textures and facies associations often result from, or are susceptible to, diagenetic
263 recrystallization which, in the presence of organic remineralization, can impart more negative
264 and scattered isotopic values. We note that $\delta^{18}O_{carb}$ isotopic values of the Pilgrimage Road
265 section are not more negative than the other two sections (see Supplementary Data Table).
266 Broadly, however, the stratigraphic trends measured at Pilgrimage Road resemble those at
267 Arroyo Pedroche. In any event, the Pedroche Formation, as defined by lithostratigraphy,
268 encompasses diachronous carbonate deposition.
269 The global boundary stratotype section and point (GSSP) for the Cambrian
270 Terreneuvian–Series 2 boundary remains under consideration by the International
271 Subcommission on Cambrian Stratigraphy (Peng and Babcock, 2011). Most workers propose to
272 define this boundary at the first appearance datum of trilobites (Zhu et al., 2006; Babcock and
273 Peng, 2007; Peng and Babcock, 2011) or various SSF taxa (Rozanov et al., 2011; Steiner et al.,
274 2011). However, the concept of the first appearance datum has been criticized for potential
275 globally diachroneity (Landing et al., *in press*), due either to lithofacies-/sequence stratigraphic-

bound fossil distribution (see, for instance, Holland, 1995) or provincialism and delayed ecological dispersion. For these reasons, Landing et al. (*in press*) propose to tie the Terreneuvian–Series 2 boundary to the positive $\delta^{13}C_{carb}$ excursion IV within the lower Atdabanian Stage of Siberia. The chemostratigraphic framework developed here for the trilobite, archaeocyath, and small shelly fossil bearing Pedroche Formation will assist in the correlation of the Ovetian Stage to other regions in which high-resolution biostratigraphy can be linked to chemostratigraphy. However, the uncertainty in correlating the Pilgrimage Road section to the Arroyo Pedroche type section—just kilometers away—provides a note of caution in applying chemostratigraphy to boundary definition. Without question, the strongest correlations—and, hence, boundary definition—will occur when bio- and chemostratigraphic data are considered together.

5. LITHOFACIES DESCRIPTIONS and PALEOENVIRONMENTAL INTERPRETATIONS

In the follow section, we describe the lithofacies of the Pedroche Formation, document the association of these lithofacies within each of the three measured stratigraphic sections and interpret the paleoenvironment of deposition. This sedimentological and stratigraphic framework will provide the context for quantifying the skeletal contribution to, and petrographic textures of, the carbonate lithofacies of the Pedroche Formation.

5.1 Lithofacies descriptions

5.1.1 Thrombolite (facies A) and associated nodular limestone (facies B)

Calcimicrobial thrombolite (facies A; Fig. 3), herein referred to as thrombolite, occurs with the characteristic mega- to meso-scale structures defined by Shapiro (2000). The simplest macrostructures appear as isolated, subspherical patches or 'head-like-shapes' (facies A-0; Fig. 4), 15-20 cm wide and up to 40 cm high, with densely packed, irregular-shaped mesoclots (1-2 cm wide; mesostructure 'a'; Fig. 4). These thrombolite heads occur interbedded with finely laminated siltstone, sandstone and thin lenses of ooid grainstone (Fig. 4**;** see Section 5.1.2). Most commonly, thrombolite heads nucleated atop ooid grainstone lenses. These thrombolite heads are smaller than those described as calyptra mounds by James and Debrenne (1980).

Commonly, thrombolites aggraded to meter-scale megastructures within the Pedroche Formation, and these are characterized by both biohermal and biostromal geometries. Here, we subdivide Pedroche thrombolite bioherms according to their size, coeval facies-relationships and internal structure. The largest bioherms (facies A-I and A-II; Fig. 4), up to 2-3 m in diameter and 2.6 m high, resemble complexes elsewhere described as 'dilophoids' (see review in James and Debrenne, 1980). These geometries aggrade through the lateral and vertical stacking of smaller, subspherical head-like forms, generally 20-25 cm in diameter (facies A-I; Fig. 4), but up to 50 cm in diameter toward the tops of bioherms (facies A-II; Fig. 4). Small heads display dense, irregular-shaped mesoclots (1-2 cm wide; mesostructure 'a'; Fig. 4) whereas the largest heads include large, irregular mesoclots (10-15 cm wide; mesostructure 'd'; Fig. 4) that may contain archaeocyaths (mesostructure 'e'; Fig. 4). Within bioherms, individual thrombolites heads are surrounded by siltstone (Figs. 3b and 4). Moreover, larger bioherms occur as both isolated aggradations and as laterally and vertically stacked 'stratigraphic reefs' (*sensu* Dunham, 1970).

Bioherms (facies A-I and A-II; Fig. 4) grade laterally into nodular limestone and fine siltstone interbeds. The nodular limestones (facies B; Fig. 4) have a mottled texture imparted by

322 the high density of small, rounded thrombolite mesoclots (<5 mm, commonly ~ 2 mm;
323 mesostructure ‘b’; Fig. 4). Toward the top of some bioherms, the mesostructure of nodular
324 limestone includes columnar/digitate mesoclots, some of which branch (mesostructure ‘c’; Fig.
325 4). These columnar and digitate mesoclots may be scoured by oolitic grainstone. The largest
326 bioherm complexes are usually onlapped by parallel laminated siltstone and sandstone and ripple
327 cross-bedded sandstone, revealing cm- to decimeter-scale synoptic relief during bioherm
328 accretion.

329 Small bioherms (facies A-III; Fig. 4), usually 1 m in diameter and up to 1 m in height
330 (Fig. 3a), have an internal structure equivalent to A-I bioherms composed of small, irregular
331 mesoclots (mesostructure ‘a’; Fig. 4). Like their larger counterparts, these bioherms commonly
332 nucleated above channelized lithosomes of ooid and oncoid grainstone (facies C2 below). Ooid
333 channel deposits (up to 70 cm thick), wavy-to-hummocky laminated siltstone and ripple cross-
334 bedded sandstone drape and flank the margins of small bioherms, and interbed laterally with
335 small bioherms.

336 Biostromal geometries occur as plano-convex, lenticular beds up to 2 m-wide and 60 cm-
337 thick (facies A-IV; Fig. 4) and as thick, vertically stacked, tabular beds (facies A-V; Fig. 4).
338 Lenticular biostromes display an internal structure composed of small, sub-spherical heads of
339 densely packed, irregular mesoclots (mesostructure ‘a’; Fig. 4) and, rarely, larger heads with
340 large, irregular mesoclots with rare archaeocyaths (mesostructure ‘e’; Fig. 4). These lenticular
341 biostromes commonly appear above the top of coarsening- and thickening-upward sequences of
342 finely laminated siltstone to interbedded siltstone and sandstone to hummocky cross-bedded
343 sandstone. They also occur above thin, massive lenses (facies C1), small, channelized lithosomes

(facies C2), and planar cross-bedded tabular beds (facies C3) of ooid and oncoid grainstone (see Section 5.1.2).

Tabular biostromes do not display the characteristic internal structure of amalgamated subspherical heads. Rather, these beds display a massive internal texture with diffuse, wavy silt intercalations, fenestral cavities (up to 2 cm wide), a variable density of mesoclots, and irregular red sedimentary infillings (Fig. 4; mesostructures 'h', 'i' and 'j'). Red infillings appear to be composed of iron-rich dolomicrite and do not host iron-oxyhydroxides. Outcrop observations suggest that fenestral cavities account for 5% to 20% of tabular biostrome beds whereas the red irregular infillings may comprise up to 30-40% of these beds. Some thick biostromal beds show an increase in the density of mesoclots, silt content, and fenestral and irregular cavities from the base to the top of each bed (Fig. 4; gradational transition from 'h' to 'j'). Accompanying the increase in red, sedimentary infillings, tabular biostrome beds show a characteristic vertical change from grayish to reddish colors. Large, irregular mesoclots with archaeocyaths (mesostructure 'e') may also occur. Thrombolite biostrome tops occasionally develop columnar stromatolites that interfinger laterally with ooid grainstone.

In thin-sections with exceptional fabric retention, petrography reveals that thrombolite mesoclots are composed of the calcimicrobes *Epiphyton*, *Renalcis* and, rarely, *Girvanella* that appear as both intergradations and intergrowths from one morphotype to another at a sub-mm scale (Fig. 5a,b; Pratt, 1984). Aggrading neomorphism and/or secondary dolomitization obscures the primary texture of the matrix between micritic mesoclots. Crenulated-to-wispy dissolution seams with siliciclastic and iron oxide stylocumulate are common to this lithofacies. Millimeter-wide veins of coarse calcite spar often dissect the thrombolite lithofacies.

366 Within the thrombolite facies, archaeocyath fossils occur both surrounded by the grey,
367 micrite matrix between mesoclots (mesostructure ‘d’; Figs. 3d and 4) and within large mesoclots
368 (mesostructure ‘e’). The maximum density of archaeocyaths in thrombolite facies was observed
369 in *ex situ* blocks at the Arroyo Pedroche section (Fig. 2, covered interval between 68 m and 81
370 m) that were displaced during construction of a local road. These *ex situ* blocks comprise
371 mesostructures ‘f’ and ‘g’ (Fig. 4), and large irregular mesoclots are surrounded by mm- to cm-
372 scale lenses of siltstone and ooid grainstone. Within these blocks archaeocyaths developed a
373 secondary branching modular framework (described by Moreno-Eiris, 1987a,b,c,d) and we
374 estimate, based on outcrop appearance, that archaeocyaths account for up to 20-30% of rock
375 volume. In general, however, and throughout *in situ* strata of our measured sections,
376 archaeocyaths represent a more minor component of this lithofacies.
377
378 *5.1.2 Ooid, oncoid and peloid grainstone (facies C)*
379 Lithofacies C consists of light grey to mauve weathering, medium-to-thick beds of well-
380 sorted ooid, oncoid and/or peloid grainstone (Fig. 6). These grainstone beds occur with massive,
381 lenticular geometries (facies C1; Fig. 4); as channelized lithosomes (facies C2; Fig. 4); and as
382 tabular beds with planar cross-bed sets (facies C3; Fig. 4). Individual ooids range from 0.5–1.0
383 mm in diameter (Fig. 6a). Petrographic examination reveals three distinct cortical fabrics. Most
384 commonly, ooids display a fabric-destructive dolomitization by euhedral crystals (Fig. 7a-c).
385 This texture indicates dissolution of the primary cortical mineralogy, leaving casts of nearly
386 circular morphology later filled with dolomite cement (oomolds). More rarely, ooids have a
387 micritized cortex (Fig. 7d). In some instances, these reveal faint concentric laminations and/or
388 the ghosts of radially oriented crystals (Fig. 7e), suggesting that micritization occurred at the

389 expense of the primary cortical fabric. Under cross-nichols, micritic ooids display a pseudo-
390 uniaxial extinction cross. Regardless of preservation texture, few ooids retain discernible nuclei
391 (Fig. 7). Such an absence suggests a nucleus of carbonate that dissolved along with the primary
392 cortices. Rarely, the interiors of dolomitized ooids include a cluster of equant, anhedral
393 microspar crystals, suggesting, perhaps, that ooids nucleated from peloids (Fig. 7b).
394 We observed a second set of structureless, micritized grains, 0.1–1.0 mm in diameter,
395 with morphologies that deviate from spherical. We classified these as peloids. Peloids are
396 generally ovoid, whereas coarse-grained peloids appear nephroid and, rarely, irregular in outline
397 (Fig. 7f). A fibrous, isopachous cement often envelopes individual grains, displacing an inferred
398 primary grain-to-grain contact (Fig. 7). Given the history of fabric-destructive recrystallization
399 apparent from ooid textures, it is possible that grains classified as peloids based on their
400 preserved texture originated as oncoids. Alternatively, some of these peloids may be superficial
401 ooids that nucleated around irregularly shaped skeletal grains. Unambiguous oncoids are present
402 as mm–cm-scale, oblate-to-irregular shaped, sub-rounded micritized grains (Fig. 6b).
403 Skeletal clasts are rare within the ooid/oncoid/peloid grainstone facies (Fig. 5). Within all
404 samples thin-sectioned, only trilobites (Fig. 5c), calcitic brachiopods (Fig. 5d) and SSFs (Fig. 5e)
405 were identified within the grainstone lithofacies; archaeocyaths were absent from bioclastic
406 debris. When present, skeletons and bioclasts are molded by an equant, microspar, and are
407 commonly enveloped by isopachous cements (Fig. 5). Trilobite carapaces and cortoids of
408 trilobite incurved margins are replaced by rectangular-to-blocky dolomite (Fig. 5c).
409
410 *5.1.3 Interbedded carbonate mudstone; bioclastic wackestone; archaeocyathan floatstone*,
411 *packstone*, and *rudstone; and siliciclastic siltstone (facies assemblage D)*

412 Facies assemblage D consists of massive, neomorphosed carbonate mudstone; bioclastic
413 wackestone; and intergrading archaeocyathan floatstone, packstone and rudstone interbedded
414 with abundant crenulated-to-stylolitic, parallel, sub-parallel, and anastomosing laminae and beds
415 of red siliciclastic siltstone imparting an amalgamated stylonodular to stylobedded fabric (Figs. 4
416 and 8a-c). Individual facies occur either with gradational-to-sharp contacts over a cm-to-mm
417 scale, or as micronodules delineated by dissolution seams enriched in siliciclastic stylocumulate.
418 Field observations indicate that carbonate comprises ~50–80% of this lithofacies, averaging 60–
419 70%; however, for short stratigraphic intervals, siltstone laminae and beds may comprise up to ~
420 80% of rock volume. Rarely, these lithologies compose the clasts of intraclastic breccias.
421 Archaeocyath clasts, which range from 0.5–3 cm in diameter, are oriented randomly and aligned
422 along their elongate axis (Fig. 8b,c).
423 Petrography reveals three distinct neomorphic carbonate spar fabrics. The first is an
424 inequigranular, xenotopic, reddish-pink microspar hosting 5–10% brown-to-opaque, rectangular,
425 silt-sized clay mineral grains and sub-rounded Fe-oxide crystals, perhaps after pyrite (mcr1; Fig.
426 8d). This fabric is interpreted as a neomorphosed silt-bearing micrite. A second common fabric
427 comprises a drusy-to-equant mosaic of xenotopic microspar lacking siliciclastic grains but, at
428 times, hosting < 5% light-green, rectangular lathes of glauconite (mcr2; Fig. 8e). This fabric
429 represents a variably fabric destructive to fabric retentive early burial cement. Less commonly, a
430 third fabric of equigranular, hypidiotopic-to-idiotopic coarse spar with twinned-lamellae occurs
431 as pockets within fabric mcr2, forms recrystallization halos around archaeocyath clasts, or veins
432 that cross-cut other matrix fabrics (sp; Fig. 8f). We interpret this fabric to have formed during
433 later stage fluid flow that neomorphosed the drusy cement, with flow preferentially running
434 through high porosity conduits provided by archaeocyath skeletons.

435 Archaeocyath skeletal preservation occurs through multiple pathways (Fig. 9). Drusy
436 microspar (mcr2, but lacking glauconite) typically molds the outer wall, inner wall and septa of
437 individual archaeocyaths (Fig. 9b-d). Rarely, microcrystalline hematitic overgrowths, known as
438 frutexites, rim the exterior of the outer wall (Fig. 9a). (Frutexites has been described from
439 Proterozoic to Recent marine, continental and subterranean depositional environments within
440 stromatolites, hardgrounds, microbial limestones, cavities, caves and Neptunian dikes; most
441 authors consider Frutexites to be a bacterial-induced texture; see review by Rodríguez-Martínez
442 et al., 2011). Commonly, a slightly coarser drusy microspar (mcr2) or an optically twinned,
443 coarse spar (sp) molds the intervallum (Fig. 9c,d); more rarely, the intervallum may be filled
444 with reddish-pink microspar (mcr1; Fig. 9b) or include both mcr1 and mcr2 within the same
445 specimen (Fig. 9c). Likewise, the central cavity may be infilled by mcr1 (Fig. 9b,c); however,
446 more commonly among smaller specimens, a drusy microspar (mcr2) or a coarse spar (sp; Fig.
447 9d) molds the central cavity. The petrogenesis of archaeocyath preservation is apparent from
448 Figures 9b and 9c. Post-mortem, the intervallum and central cavity of archaeocyath clasts were
449 filled, to varying degrees, by siliciclastic-bearing carbonate silt (mcr1). Subsequently, primary
450 skeletal porosity was occluded by a drusy microspar cement (mcr2) or coarse spar (sp).
451 Small shelly fossils are always molded by a drusy microspar (mcr2; Fig. 10). Within this
452 lithofacies, microbial fabrics are rare but, when present, include mm-scale hematitic
453 stromatolites (Fig. 9a) and filamentous, oncolitic halos around archaeocyath bioclasts (Fig. 9b).
454 No echinoderm ossicles, and few trilobite carapaces, were observed within representative thin-
455 sections of this lithofacies.
456
457 *5.1.4 Massive grainstone and recrystallized carbonate*

458 This facies consists of thin to thick tabular or irregular-to-wavy beds of very fine- to
459 medium-grained grainstone, nodular carbonate and thick to very-thick beds of massive, and
460 finely-to-coarsely recrystallized and/or vuggy dolomitized carbonate.
461
462 *5.1.5 Fine-grained siliciclastic rocks*
463 This facies consists of very-thin to thin beds of shale and planar laminated and ripple
464 cross-laminated siltstone as well as thin to medium, planar-to-undulose beds of very fine to
465 medium-grained, micaceous quartz sandstone which may be massive, planar laminated, ripple
466 cross-laminated, or swaley-to-hummocky cross-laminated and cross-stratified.
467
468 *5.2 Lithofacies associations*
469
470 *5.2.1 Cerro de Las Ermitas section*
471 At the Cerro de Las Ermitas study area, carbonates of the Pedroche Formation
472 transgressed over and infilled meter-scale paleotopographic relief incised into andesite of the
473 underlying San Jerónimo volcano-sedimentary complex (Fig. 2). A complex cavity-dwelling
474 calcimicrobial and skeletal community found on this paleosurface is described thoroughly by
475 Vennin et al. (2003) and Perejón and Moreno-Eiris (2007).
476 Within the same study area, a decameter-scale bioherm directly, but unconformably,
477 overlies these andesites (Zamarreño and Debrenne, 1977; Moreno-Eiris, 1987). Moreno-Eiris
478 (1987) differentiated seven lithofacies along three stratigraphic transects: i) polymictic
479 conglomerates (with rounded, pebble- to boulder-size clasts of andesite, metaquartzite and shale)
480 and violet siltstone; ii) micaceous, quartz-rich, laminated siltstone; iii) siltstone with calcareous

nodules; iv) micritic limestone; v) reefal limestone (up to 12 m thick) and small calcimicrobial mounds; vi) nodular peri-reefal limestone; and vii) carbonate sedimentary breccia. The Cerro de Las Ermitas stratigraphic section of this study (LE; Figure 2) partially overlaps the section described by Moreno-Eiris (1987; section VII', up to their 40 m). The interbedded carbonate mudstone, bioclastic wackestone and archaeocyathan floatstone, packstone and rudstone and siliciclastic siltsone lithofacies assemblage (facies D) of this study corresponds to the nodular peri-reefal limestone and siltstone with calcareous nodules facies assemblage described by Moreno-Eiris (1987). We note that while our Cerro de Las Ermitas section did not directly transect an archaeocyathan framework reef, bioherms were observed directly above the section. We do not include these bioherms in our measured section because dense vegetation precluded confident stratigraphic placement.

5.2.2 Cerro de Las Ermitas environmental interpretation

The interlaminated fine-grained carbonate (mudstone and wackestone) and siliciclastic siltstone lithologies accumulated predominately through the settling of suspended fine grains during very low energy conditions. The changing abundance of carbonate versus siliciclastic silt reflects the temporally variable influx of terrigenous material diluting and/or suppressing background carbonate production. In contrast, coarse-grained carbonate lithologies reflect higher-energy depositional episodes that entrained reef organisms, re-worked and winnowed them, as evidenced by deposits of parallel-oriented whole and partial archaeocyath clasts (Fig. 8b). Localized brecciation within this lithofacies likely resulted from the collapse of the flanks of over-steepened calcimicrobial reefs. We interpret this lithofacies assemblage as an inter-reef and reef-flank (talus) deposit.

504

505 *5.2.3 Pilgrimage Road section*

506 The Pedroche Formation is ~133 m thick at this stratigraphic section; however, there are
507 no biostratigraphic zonations determined for this section to correlate to the Arroyo Pedroche or
508 Cerro de Las Ermitas sections. Within this section, the lowermost strata of the Pedroche
509 Formation (0–45 m) are dominated by siliciclastic facies with minor interbeds of carbonate.
510 These siliciclastic lithologies are stacked in meter-scale parasequences of planar and ripple cross-
511 laminated siltstone and very fine- to fine-grained micaceous quartz sandstone with and without
512 lime mudstone nodules. Flaser bedding occurs rarely within the basal 25 m of the section. Beds
513 of massive and ripple cross-bedded fine- to medium-grained quartz sandstone, beds and lenses of
514 massive (facies C2) and ripple cross-bedded (facies C3) ooid/oncoid/peloid grainstone and
515 thrombolites (facies A-0 and A-IV) intercalate with these fine-grained siliciclastic lithologies.

516 At ~45 m, the carbonate mudstone nodules within a 2.5 meter-thick siltstone/sandstone
517 bed increase in abundance, grading into a carbonate interval from 47.5 – ~71 m. Carbonate
518 textures within this interval include: interbedded massive recrystallized limestone; vuggy,
519 coarse-crystalline dolomite; and one ~3 meter-thick massive, recrystallized thrombolite (facies
520 A-II).

521 Cyclic interbedding of lithofacies occurs from ~71 m to the top of the measured section.
522 (Here, we use the term cycle to describe repetition of lithologies, not to invoke a particular time-
523 scale or depositional mechanism (*sensu* Myrow et al., 2012).) At Pilgrimage Road, cycles
524 include: (1) micaceous siltstone and very fine-grained quartz sandstone, (2) massive to cross-
525 bedded ooid/oncoid/peloid grainstone (facies C2 and C3) followed by (3) very thick, massive
526 thrombolite biostrome (facies A-V) interbedded and draped with siltstone. Variations on this

527 generalized lithologic cycle include the absence of either the fine-grained siliciclastics or the
528 ooid/oncoid/peloid grainstone lithofacies. The thrombolite facies contains rare archaeocyaths.
529 Zamarreño (1977) described the cyclic interbedding of these lithofacies, as well as the geometry
530 of thrombolite mounds, in further detail.
531
532 *5.2.4 Arroyo Pedroche section*
533 Previously, the Arroyo Pedroche section was divided into two members (Perejón et al.
534 1996), and here we focus our work on Member 1. The Arroyo Pedroche section comprises mixed
535 siliciclastic and carbonate lithologies, both non-cyclically and meter- to decameter-scale
536 cyclically (serially repeated) bedded (Fig. 2). At Arroyo Pedroche, the lowermost ~19 m of the
537 Pedroche Formation consist of shale and siltstone with minor intercalations of thrombolite
538 (facies A-0 and A-IV), nodular limestone (facies B) and ooid/oncoid/peloid grainstone (facies
539 C1). Towards the top of this interval, ripple and hummocky cross-stratified siltstone and fine- to
540 medium-grained sandstone beds occur interbedded with rare beds of massive ooid grainstone
541 (facies C3). Massive, recrystallized carbonate crops out between 19 and 31 m, yet relict textures
542 within this interval indicate a primary thrombolitic texture (facies A-1).
543 From 31–39 m, the Pedroche Formation records the vertical accretion of six thrombolite
544 bioherm complexes (facies A-I and A-II) that grade laterally into, and intercalate with, nodular
545 limestone (facies B) and parallel laminated shale and siltstone. Thrombolite bioherms nucleated
546 atop both siliciclastic beds and ooid/oncoid/peloid grainstone channel deposits (facies C2).
547 Generally, parallel and ripple cross-laminated, very fine-grained sandstone onlaps these bioherm
548 complexes, but occasionally ooid/oncoid/peloid grainstone channels scoured the top and margin
549 of bioherms.

From ~40 – 50 m, the section comprises non-cyclic intercalations of: (1) planar laminated shale and siltstone, and planar laminated to ripple cross-laminated very fine-grained sandstone; (2) beds, channels (facies C2), and lenticular bars (facies C3) of ooid/oncoid/peloid grainstone; and (3) isolated and amalgamated thrombolite bioherms (facies A-III) typically surrounded by bedded, fine-grained siliciclastic lithologies.

The stratigraphic interval from 50–60 m corresponds to a coarsening- and thickening-upward succession of finely laminated siltstone, parallel and ripple cross-laminated sandstone and hummocky cross-stratified sandstone. Lenticular thrombolites (facies A-IV) nucleated above these sandstone beds and were capped by finely-laminated siltstone. The final development of thrombolite bioherms (facies A-III and A-II) at the Arroyo Pedroche section, from ~60–65 m and in *ex situ* blocks within a covered interval up to 81 m, aggraded in association with ooid/oncoid grainstone (facies C3) and were subsequently draped by siltstone laminae that grade upwards into trough cross-stratified sandstone.

Cyclic interbedding of facies is more strongly developed from 81–92 m. These cycles consist of a basal, siliciclastic-dominated interval and an upper, carbonate-dominated interval. The generalized succession of siliciclastic lithologies within cycles includes: (1) interbeds of laminated shale and siltstone and/or (2) interbeds of laminated-to-swaley siltstone and very fine-grained sandstone grading into (3) swaley, hummocky, or ripple cross-laminated, very fine- to medium-grained, amalgamated sandstone. In turn, the coarser, cross-stratified siliciclastic lithologies are commonly interbedded with, or overlain by, carbonate facies that may include: (4) cross-bedded or massive ooid/peloid/oncoid grainstone and (5) lenticular thrombolites (facies A-IV). Broadly these mixed siliciclastic-carbonate cycles represent upward-coarsening cycles. We note, however, that interbedding of siliciclastic lithologies may occur without a discernible

coarsening-upward succession, or instead, display a distinct fining-upward succession. In this upper cyclic section, wispy-to-crenulated physical dissolution seams with siliciclastic stylocumulate are common within carbonates, and increase in density near cycle tops.

Throughout the remaining strata of the Arroyo Pedroche section (92–138 m), thrombolite biostromes (facies A-V) are common and nucleate from massive to planar cross-bedded ooid/oncoid/peloid grainstone (facies C3) and, more rarely, sandstone beds. Within this interval, the transition from thrombolitic to columnar stromatolitic texture near the top of bioherms is common. Generally, however, thrombolites display typical mesostructure fabrics with fenestral cavities (Fig. 4).

5.2.5 Arroyo Pedroche and Pilgrimage Road environmental interpretations

Facies associations of the Pedroche Formation at the Pilgrimage Road and Arroyo Pedroche sections reveal broadly similar depositional environments. The base of both stratigraphic sections record predominantly siliciclastic sedimentation with only minor carbonate interbeds. Within the Arroyo Pedroche section from 0–14 m, the interlaminated and interbedded shale, siltstone and fine-grained sandstone beds without macroscopic sedimentary structures indicate suspension deposition of siliciclastic particles entrained in dilute turbidity currents. We interpret these lithologies to record sediment accumulation in an offshore shelf or distal ramp setting. In contrast, the introduction of macroscopic sedimentary structures within siltstone and sandstone above 14 m—including hummocky, swaley and ripple cross-lamination—record traction deposition from gravity waves. Such sedimentary structures within well-sorted, amalgamated beds are common in shoreface depositional environments. Thus, the base of the

595 Arroyo Pedroche section records an upward-shoaling succession from a calm, deep-water setting
596 to a shoreface environment influenced by tide, wave and storm activity.

597 The basal meter-scale siliciclastic-parasequences of the Pilgrimage Road section (0–45
598 m) include parallel and ripple cross-laminated siltstone and sandstone, and wavy and flaser
599 bedding structures. Like the Arroyo Pedroche section, the minor interbeds of massive lenses of
600 ooid grainstone (facies C3), here interpreted as storm-induced gravity flow deposits, and the
601 aggradation of isolated thrombolites (facies A-0 and A-IV) represent the maximum advance of
602 the carbonate system onto the middle/upper shoreface. We interpret the lower ~25 meters of the
603 Pilgrimage Road section, below the common occurrence of thrombolites, to record a shallowing
604 upward succession displaying an increase in higher-energy facies (e.g., wave-rippled siltstone,
605 sandstone and ooid/oncoid grainstone) and a reduction of fine-grained, suspension settled
606 siliciclastic input. However, this shallowing resulted in deposition transitioning from
607 lower/middle to upper shoreface conditions rather than from offshore to shoreface deposition as
608 recorded within strata at the Arroyo Pedroche section. At Arroyo Pedroche, this shallowing
609 preceded the maximum development of laterally and vertically stacked thrombolite bioherms
610 with centimeter- to decimeter-scale synoptic relief (31–39 m). At Pilgrimage Road, this
611 shallowing preceded the deposition of carbonates for which recrystallization has since destroyed
612 primary textures. Hence, we do not offer an interpretation of depositional environment for these
613 strata.

614 We interpret the depositional environment of Arroyo Pedroche strata from 31–49.5 m as
615 a thrombolite mound-and-channel facies. Here, fine-grained siliciclastic lithologies onlapped
616 onto, and scoured the margins of, thrombolites bioherms. The continuous disaggregation and
617 erosion of thrombolite into small, rounded micritic grains (peloids) contributed to accumulation

618 of nodular limestone (facies B) surrounding the bioherms. In turn, both the thrombolite bioherms
619 and the surrounding peloidal, nodular limestones were sporadically scoured by channelized ooid
620 and oncoid deposits.

621 Massive, planar-laminated and ripple cross-laminated, undulatory-bedded carbonate
622 grainstone, and massive carbonate without discernible texture, record a combination of traction
623 transport and suspension deposition. These lithologies are common in shallow, subtidal
624 depositional environments. Well-sorted, cross-bedded ooid/oncoid/peloid grainstone beds reflect
625 traction deposition from high-energy flow capable of winnowing carbonate and siliciclastic mud,
626 silt and fine sand grains. We interpret these lithologies as migrating shoals and/or sheets that
627 prograded onto deeper subtidal lithologies (i.e., siliciclastic sands and thrombolite bioherms).

628 Within both the Arroyo Pedroche and Pilgrimage Road sections, the reduction in
629 siliciclastic influx likely facilitated the colonization of the seafloor by calcimicrobial
630 communities and the aggradation of thrombolites (facies A-0 and A-IV thrombolites found
631 within the basal meters of both sections). The migration of siliciclastic sand shoals and ooid
632 channels and shoals influenced the geometry of thrombolite growth. Large thrombolite bioherms
633 (facies A-I and A-II) accreted during coeval suspension deposition of silts. In contrast, the lateral
634 and vertical accretion of small bioherms (facies A-III) was stymied by the physical erosion and
635 cessation of carbonate production by migrating siliciclastic sand shoals and subtidal oolitic
636 channels. The presence of swaley and hummocky cross-laminae within siliciclastic sandstone
637 reflects wave-generated bedforms developed during storms. In the intervening calm periods, the
638 sandy seafloor was continually and densely recolonized by calcimicrobes, allowing lenticular
639 thrombolites to develop, before subsequent influxes of suspended siliciclastic sediment
640 smothered them during storms.

We interpret the uppermost meter-scale thrombolite bioherms (facies A-II and A-III) at the Arroyo Pedroche section to have grown in a shallow, protected back-shoal environment behind and between ooid/oncoid/peloid bar deposits (facies C3). The widespread development of fenestral cavities within these bioherms, the increase in silt intercalations within thrombolitic textures, and the transition from thrombolite to columnar stromatolite at the top of these bioherms all support the interpretation of a shallow, back-shoal environment.

The interfingering and interbedding of siliciclastic sands, oolitic carbonates, and thrombolite bioherms within the mound-and-channel environment speaks to a contiguous spatial distribution of these lithofacies along an ancient mixed siliciclastic–carbonate shoreface. Evidence for subaerial exposure is absent in both sections. From this, we interpret that sediment influx did not consistently outpace the creation of accommodation space. Likewise, the common occurrence of macroscopic sedimentary structures formed from traction deposition indicates that the creation of accommodation space did not significantly outpace sediment accumulation, which would result in shoreface retrogradation and transition into an offshore depositional environment. Thus, we interpret the alternation between siliciclastic-dominated and carbonate-dominated sedimentation within the mound-and-channel facies to reflect the lateral migration of lithofacies rather than major changes in accommodation space and facies belts.

In contrast, when mixed siliciclastic–carbonate lithologies occur together in continuous, upward-coarsening cycles (as above 81 m at Arroyo Pedroche, and above 71 m at Pilgrimage Road; Fig. 2), we interpret these as upward-shoaling successions. Above the major covered interval at Arroyo Pedroche, the basal medium-grained sandstone (81 m) of the cyclic-interbedded section includes hummocky cross-stratification. The re-introduction of this sedimentary structure indicates a deepening to a storm-dominated shoreface. Above this cycle,

664 both the transgressive siliciclastics that define the base of each cycle and the overlying ooid
665 grainstone beds include ripple cross-stratification indicative of deposition above fair-weather
666 wave base. We note, however, that the deviations from simple upward-coarsening siliciclastic
667 successions, such as fining-upward patterns or frequent alternations between suspension and
668 traction deposited sediments, reflect a more complex sediment accumulation pattern than simple
669 shoreface progradation.

670 The architecture of thrombolite facies changes significantly between the lower and upper
671 portions of both the Arroyo Pedroche and Pilgrimage Road sections. Within the basal ~71 m at
672 AP, and the basal ~45 m at PR (Fig. 2), both intervals of siliciclastic-dominated offshore to
673 lower shoreface deposition, thrombolites aggraded as bioherms with significant synoptic relief.
674 In contrast, in the upper, cyclically bedded stratigraphy, thrombolite facies developed with
675 biostromal geometries, often interbedded with siltstone. Biohermal thrombolites can aggrade
676 when water depth exceeds synoptic relief. As a corollary, the development of biostromal
677 morphologies could reflect limited accommodation space, characteristic of very shallow to
678 nearly emergent depositional environments. However, the presence of siliciclastic silt
679 interlaminae and drapes disrupting the aggradation of thrombolite bioherms and biostromes
680 suggests that the morphology of thrombolite accretion was also controlled by the relative rates of
681 carbonate precipitation versus siliciclastic influx (Cowan and James, 1993; see analogous
682 discussion of stromatolite aggradation in Grotzinger and Knoll, 1999). Thus, rather than strictly
683 associate thrombolite facies architecture with a flow-regime or water depth, we assume that
684 siliciclastic influx also influenced the morphology of thrombolite accretion. The common
685 occurrence of ooid/oncoid/peloid grainstone and sandstone beds underlying thrombolites

686 suggests that a rough substrate and a slightly elevated stable surface were favorable conditions
687 for colonization of the seafloor by calcimicrobes and subsequent thrombolite growth.
688
689 **6. THE CHARACTER OF PEDROCHE FORMATION CARBONATES**
690
691 *6.1 Carbonate versus siliciclastic lithofacies of the Pedroche Formation*
692
693 The percent contributions of carbonate lithofacies to the three stratigraphic sections of the
694 Pedroche Formation are reported in Table 1. Thrombolite facies comprise 27% and 26% of the
695 Arroyo Pedroche and Pilgrimage Road sections, respectively. Ooid/oncoid/peloid grainstone
696 comprise 3% and 6% of the AP and PR sections, respectively. Other carbonates (i.e., massively
697 recrystallized strata) account for 14% and 15% of the AP and PR sections, respectively.
698 Siliciclastic lithologies make up the remaining 56% and 53% of the AP and PR sections,
699 respectively. When calculated on a carbonate-normalized basis, thrombolites, ooid/oncoid/peloid
700 grainstone, and other carbonate lithofacies make up 60%, 8% and 32%, respectively, of the AP
701 section and 55%, 13% and 31%, respectively, of the PR section.
702 Given the mm- to cm-scale transition between lithologies in the interbedded carbonate
703 mudstone, bioclastic wackestone, archaeocyathan floatstone–packstone–rudstone and siliciclastic
704 siltstone lithofacies (facies assemblage D) of the Cerro de Las Ermitas section, we do not attempt
705 to quantify the percent siliciclastics versus carbonates, or the percent of individual carbonate
706 lithologies beyond the field observation estimates reported with the lithofacies descriptions.
707

6.2 Quantifying skeletal contributions to, and fabric components of, carbonate facies of the Pedroche Formation

Our raw point-count data are summarized in Table 2. In the following discussion, we report the calculated average percentage of a constituent skeletal or fabric component within a lithofacies unless otherwise noted (summarized in Table 3).

The percentage of skeletal material contributing to carbonate lithofacies of the Pedroche Formation, as determined from the point count data in Table 2, is shown in Fig. 11. Total skeletal contribution peaks at 21.5% (average 18%; Fig. 11a) in thin-sections identified as archaeocyathan floatstone, packstone or rudstone lithologies within facies assemblage D. In contrast, total skeletal contributions to thin-sections classified as bioclastic wackestone or carbonate mudstone in facies assemblage D range from 3–9% and 0–2%, respectively (Fig. 11a). Within the archaeocyathan floatstone–packstone–rudstone lithofacies, archaeocyaths are more abundant than SSFs (Fig. 11b), with archaeocyaths averaging 11% and SSFs averaging 4%. In contrast, within bioclastic wackestone and carbonate mudstone lithofacies, archaeocyaths are, on average, less abundant than SSFs (Fig. 11c). No thin sections of the thrombolite facies included a quantifiable skeletal contribution (Fig. 11a). Likewise, of the ooid/oncoid/peloid grainstone samples analyzed, only one revealed discernible skeletal clasts (2%; Fig. 11a).

The percent composition of all quantitatively important (i.e., > ~1%) constituents of each of the carbonate lithofacies assemblages of the Pedroche Formation is depicted in Fig. 12. In addition to the variable skeletal contribution discussed above, micrite (82%) and siliciclastic clay and/or silt (8%) dominate the composition of facies assemblage D (Fig. 12a); in contrast, microbial textures (e.g., hematitic stromatolitic laminae and frutexites) contribute a maximum of

731 9%, but typically much less (0.6%; Figs. 9a and 12a). The thrombolite lithofacies is composed
732 entirely of clotted micrite (36%) set within a microspar matrix (herein interpreted as
733 neomorphosed micrite; 50%; Fig. 12b). Similarly, the ooid/oncoid/peloid grainstone lithofacies
734 is composed almost entirely of either ooids (39%), oncoids/peloids (5%, respectively) and sparry
735 cement (47%; Fig. 12c).
736
737 *6.3 Comparing the nature of carbonate production within the Pedroche Formation to other*
738 *Lower Cambrian, archaeocyath-bearing carbonate platforms*
739
740 Assignment of the Pedroche Formation to Cambrian Series 2, Stage 3 provides context
741 for comparing Pedroche carbonate production in general, and skeletal contribution in particular,
742 to contemporaneous carbonate platforms and archaeocyathan bioherms. First, however, we must
743 address how well our point-count data estimate skeletal contributions to these lithofacies. All
744 Pedroche Formation samples reveal some evidence of fabric destructive diagenesis. The subset
745 of thin-sections analyzed in detail display the least pervasive fabric-destructive diagenesis such
746 that point counts of textural fabrics and fossil occurrences should best approximate the primary
747 depositional texture. Nevertheless, the results presented here are necessarily minimum estimates
748 of the primary carbonate constituents (e.g., skeletons and coated grains) or maximum estimates
749 of secondary textures (e.g., cements). Even when primary matrix microfabrics are difficult to
750 discern, however, original skeletal elements often retain their diagnostic features (e.g., Fig. 9a).
751 Finally, we note that the most fossiliferous strata observed in our field area were *ex situ* blocks of
752 thrombolite lithofacies bearing archaeocyaths within the Arroyo Pedroche section in an interval
753 without clear biostratigraphic or chemostratigraphic relationship to the Las Ermitas section.

While the most fossiliferous samples point counted within this study approach the percent archaeocyath skeletal volumes of these *ex situ* lithologies that we estimated by eye, our point-count samples may ultimately underestimate the total skeletal abundance by several percent.

The most pervasive fabric-destructive fabrics appear in the thrombolite facies, hence our limited point-count observations (n=5). Despite field observation of archaeocyaths (and other skeletons) associated with the thrombolite lithofacies (Fig. 3d), none of the thin-sections analyzed included a quantifiable skeletal contribution (Figs. 11a, 12b). Likewise, only one thin-section from the grainstone lithofacies included a quantifiable skeletal contribution (Figs. 11a, 11c). It is possible that fabric-destructive recrystallization caused point count data to underrepresent skeletal contribution to these lithofacies. We prefer, however, the interpretation that while archaeocyath and other skeletal elements are present within this lithofacies, their absence (or low abundance) from point-count data correctly implies limited abundance or, at the most, a spatially-discrete enrichment in skeletal clasts that reflects a low total skeletal volume.

Total skeletal contribution within the archaeocyath-bearing inter-reef and reef-flank facies (assemblage D) at Las Ermitas is similar to that determined by Hicks and Rowland (2009) for microbial bioherms of the Cambrian Series 2, Stage 3–4 Xiannudong Formation, Yangtze Platform, southern China as well as by Pruss et al. (2012) for archaeocyathan patch-reefs of the Cambrian Series 2, Stage 4 Forteau Formation, southern Labrador, Canada (Fig. 13a). Likewise, the percentage of total skeletal material representing archaeocyaths (Fig. 13b) versus all other fossils (Fig. 13c) is similar between these localities, with the notable exception of higher (up to 38%) archaeocyath abundance reported by Rowland and Gangloff (1988) within microbial-boundstone of the Cambrian Series 2, Stage 3 lower Poleta Formation, western Nevada, USA. We note, however, that the percent archaeocyath abundance determined by Rowland and

777 Gangloff (1988) derives from volumetric determinations via tracing methods. Results from
778 tracing methods overestimate skeletal contribution in comparison to the grain-solid point count
779 method employed in both this study and by Pruss et al. (2012) and, therefore, cannot be directly
780 compared to these studies. More generally, Debrenne (2007) has estimated that while the percent
781 contribution of archaeocyaths to lower Cambrian bioherms can be as high as the 38% reported
782 by Rowland and Gangloff (1988) in high energy reef crests, it is more commonly 13% or less in
783 lower energy settings similar to those interpreted for the Pedroche Formation.

784 Taken together, thin-section point-counts of fossil abundance and identity within
785 Cambrian archaeocyathan–bearing inter-reef and reef-flank facies (facies assemblage D) provide
786 consistent views on reef ecology. Most lower Cambrian bioherms are calcimicrobe-bearing
787 microbialites that contain archaeocyaths. Maximum skeletal abundance is similar at the three
788 localities for which quantitative data are available (Fig. 13a), confirming previous interpretations
789 that archaeocyath-bearing microbial reefs represent important but spatially limited loci of
790 carbonate production (Rowland and Gangloff, 1988; Hicks and Rowland, 2009; Pruss et al.,
791 2012). Moreover, skeletal carbonate production is partitioned amongst archaeocyath and other
792 skeletal taxa in a consistent ratio for all three localities (Fig. 13d). Thus, if archaeocyaths were
793 not actively displacing other taxa from ecological niches, the evolution and expansion of the
794 Archaeocyatha during Cambrian Series 2 likely buoyed skeletal carbonate production beyond the
795 low diversity, low abundance observed in other places and at other times in the early Cambrian
796 (Pruss et al., 2010). Yet, even in lower Cambrian lithologies bearing archaeocyaths, skeletons do
797 not play the depositional role that they do later in the Paleozoic Era (Rowland and Gangloff,
798 1988; Hicks and Rowland, 2009; Pruss et al., 2012).

One significant difference between the Pedroche Formation and the Forteau (Pruss et al., 2012) and, to a lesser extent, Xiannudong formations (Hicks and Rowland, 2009), is the minimal occurrence of skeletal material in Pedroche grainstone lithologies. Pruss et al. (2012) found up to 20.5% (average 12.4%) skeletal material in grainstone flanking archaeocyathan reefs, whereas we found skeletons in only one thin-section (of nine analyzed) with a total skeletal contribution of 2% (Fig. 11a). Grainstone shoals and sheets represent dynamic, high-energy depositional environments where rapidly changing wave-energies often winnow skeletal fragments into coarse lag deposits. Thus, for sedimentological reasons, we might expect high variance in the skeletal contribution to grainstone facies. Pruss et al. (2012) identified echinoderms as the major constituent of grainstone skeletal debris, whereas no echinoderm fossils were observed in Pedroche Formation thin-sections. Both fossils and molecular clocks indicate an initial diversification of echinoderms during Cambrian Series 2 (Peterson et al., 2004; Bottjer et al., 2006), but early taxa appear to have been facies bound, including, in the case of helicoplacoids, to siliciclastic facies (Smith, 1985; Dornbos and Bottjer, 2000). Thus, differences from one platform to another may well reflect environmental distinctions.

6.4 Carbonate production on the Pedroche platform

The Pedroche Formation contributes to a strengthening picture of carbonate deposition on Cambrian shelves and platforms. Within the Arroyo Pedroche and Pilgrimage Road sections, thrombolite microbialites are both the most conspicuous and most abundant contributors to platform deposition, comprising 55–60% of all carbonates (Table 1). Coated grains account for 8–13% of carbonate accumulation, while the remaining 31–32% encompasses recrystallized

822 carbonate textures, and other, minor lithologies (Table 1). Skeletons, especially archaeocyaths,
823 are locally conspicuous and abundant, but because facies other than archaeocyathan rudstone
824 contain such a low skeletal component, the total measurable contribution of carbonate skeletons
825 to the platform accumulation is low, perhaps 5–6% by volume. This is not too different from
826 Cambrian samples measured in China, Newfoundland, Labrador and the North American
827 Cordillera, and well below skeletal abundances in most Middle Ordovician and younger deposits
828 (Hicks and Rowland, 2009; Pruss et al, 2010, 2012). That is, despite the fact that Pedroche
829 Formation and coeval carbonates accumulated during the acme of Cambrian body plan
830 diversification (Knoll and Carroll, 1999; Erwin et al., 2011), and despite the observation that
831 most of the skeletal designs evolved by animals appeared during this interval (Thomas et al.,
832 2000), skeletons remained a subsidiary component of carbonate deposits.
833 Clearly, Pedroche and other Cambrian carbonate accumulations are distinct from younger
834 examples. How do they compare with older platform and shelf deposits? While countless
835 stratigraphic sections transect Proterozoic carbonate platforms, few studies compile the
836 percentage of lithofacies at the outcrop-scale. Knoll and Swett (1990) reported that stromatolites,
837 oncolites and microbial laminates make up ~25% of all carbonates within the ca. 800–750 Ma
838 Akademikerbreen Group, Spitsbergen, with oolite contributing ~15%, and the remaining ~60%
839 consisting of micrite, calcarenite (carbonate grainstone), and rudstone derived from the erosion
840 and re-deposition of mostly micrite lithologies. Thus, even more than this Neoproterozoic
841 succession, microbialites represent a significant component of Pedroche carbonate accumulation.
842 Proterozoic and Cambrian carbonates differ, of course, in the *nature* of constituent
843 microbialites, being largely stromatolitic in older rocks and thrombolitic in the Cambrian Period
844 (Grotzinger, 1990; Grotzinger et al., 2000). Indeed, in the Pedroche Formation, stromatolites

make up only about 0.25% of the sedimentary package as a whole. In modern settings, thrombolites develop in subtidal environments where eukaryotic algae, especially macroscopic algae, colonize microbialite surfaces (Feldmann and McKenzie, 1998; Andres and Reid, 2006). The holdfasts of sessile benthic invertebrates might also disrupt microbial lamination (Grotzinger et al., 2000). Such observations provide a framework for interpreting Pedroche and other Cambrian thrombolites. These structures accreted subtidally, with limited influence from traction load sediments (e.g., Pratt and James 1982, 1986). Fossils and molecular clocks support the hypothesis that the diversification of green algae and sessile benthic animals contributed to the distinctive fabrics of subtidal Cambrian microbialites (e.g., Grotzinger et al., 2000). In general then, the introduction of animal and algal macrobenthos into early Phanerozoic marine communities modified the morphologies, fabrics, and facies distribution of stromatolites and thrombolites, but did not result in the elimination of microbial build-ups from carbonate platforms and shelves. That occurred later, with the mid-Ordovician radiation of heavily skeletonized sessile macrobenthos.

Increasingly, then, the Cambrian stands out as a transitional interval of carbonate deposition, with carbonate production still linked to the physical and microbial processes that had governed carbonate deposition for billions of years, but with evolving algae and animals beginning to exert a quantifiable influence on the processes, loci and fabrics of shelf and platform carbonates.

7. CONCLUSIONS

867 Carbonate carbon isotope data from three stratigraphic sections of the Pedroche
868 Formation provide the first chemostratigraphic curve for Cambrian stratigraphy of the Ossa
869 Morena geotectonic zone, Iberia. The Pedroche Formation captures the apex of an ~3‰ positive
870 $\delta^{13}C_{carb}$ excursion preceding a plateau around -1.5‰. Within the context of trilobite, small shelly
871 fossil, and archaeocyath biostratigraphy, we correlate this isotopic variability to excursion IV of
872 the Siberian Atdabanian chemostratigraphic framework, correlative to Cambrian Series 2, Stage
873 3.
874 Thrombolites and archaeocyath-bearing inter-reef and flanking-reef talus represent loci
875 for skeletal carbonate production and accumulation within the Pedroche Formation, with skeletal
876 material comprising a maximum of 21.5% of total carbonate. Of the skeletal material quantified,
877 archaeocyaths contributed an average of ~68%, with the remainder attributable to small shelly
878 fossils, trilobites, and calcitic brachiopods. The production and export of skeletal material
879 beyond these depositional environments contributed little to coeval carbonate accumulation.
880 Instead, microbial and abiotic carbonates dominated. Despite an important skeletal presence,
881 carbonate accumulation and distribution within the Cambrian Pedroche Formation appears more
882 similar to Neoproterozoic accumulations than Phanerozoic skeletal reef ecosystems.
883
884 **ACKNOWLEDGMENTS**
885 We thank the Agouron Institute for generous support as well as Daniel Schrag and Greg Eischeid
886 for access to the Harvard University Laboratory for Geochemical Oceanography, where
887 carbonate isotopic analyses were completed. We also thank Sara Pruss and an anonymous
888 reviewer for constructive criticisms that helped to improve this paper.

889 **REFERENCES**

890

891 Ábalos, B., Carreras, J., Druguet, E., Escuder Viruete, J., Gómez Pugnaire, M.T., Lorenzo
892 Álvarez, S., Quesada, C., Rodríguez-Fernández, L.R., Gil Ibarguchi, J.I., 2002. Variscan and pre-
893 Variscan Tectonics, in: Gibbons, W., and Moreno., T. (Eds.), The Geology of Spain. Geological
894 Society of London, Bath, U.K., pp. 155–183.

895

896 Andres, M.S., Reid, P.R., 2006. Growth morphologies of modern marine stromatolites; a case
897 study from Highborne Cay, Bahamas. Sedimentary Geology 185, 319–328.

898

899 Babcock, L.E., Peng, S., 2007. Cambrian chronostratigraphy: Current state and future plans.
900 Palaeogeography, Palaeoclimatology, Palaeoecology 254, 62–66.

901

902 Bard, J.P., Burg, J.-P., Matte, Ph., Ribeiro, A., 1980. La Chaîne Hercynienne d'Europe
903 occidentale en termes de tectonique des plaques, in: Cogné, J., Slansky, M. (Eds.), Géologie de
904 l'Europe. Mémoire du Bureau de Recherches Géologiques et Minières 108, pp. 233–246.

905

906 Bottjer, D.J., Davidson, E.H., Peterson, K.J., Cameron, R.A., 2006. Paleogenomics of
907 echinoderms. Science 314, 956–960.

908

909 Brasier, M.D., Rozanov, A.Yu., Zhuravlev, A.Yu, Corfield, R.M., Derry, L.A., 1994. A carbon
910 isotope reference scale for the Lower Cambrian succession in Siberia: report of IGCP project 303.
911 Geological Magazine 131, 767–783.

912

913 Cabanás, R., 1971. Observaciones sobre el Cámbrico de la provincia de Córdoba. Boletín
914 Geológico y Minero 82(3–4), 105–107.

915

916 Cabanás, R., Meléndez, B., 1966. Notas estratigráficas de la Provincia de Córdoba. Nota sobre
917 un nuevo fósil del Cambriano. Notas y Comunicaciones del Instituto Geológico y Minero de
918 España 90, 77-84.

919

920 Carbonell, A., 1926. Nota sobre los yacimientos de "Archaeocyathidos" de la Sierra de Córdoba
921 y deducción para el análisis tectónico. Boletín del Instituto Geológico y Minero de España, 3ª
922 ser., 4ª part., 47, 311–315.

923

924 Carbonell, A., 1929. Un nuevo yacimiento de Archaeocyathidae en Córdoba. Consecuencias
925 tectónicas. Memorias de la Real Sociedad Española de Historia Natural 15(1), 271–274.

926

927 Carbonell, A., 1930 a-g. Informe referente a las canteras de caliza de Majanillo y Mirabuenos,
928 desde el punto de vista de la fabricación de cemento. Revista Minera Metalúrgica y de
929 Ingeniería, 3216–3234.

930

931 Cowan, C.A., James, N.P., 1993. The interactions of sea-level change, terrigenous sediment
932 influx, and carbonate productivity as controls on Upper Cambrian Grand Cycles of western
933 Newfoundland, Canada. Geological Society of America Bulletin 105, 1576–1590.

934

935 Dallmeyer, R.D., Martínez García, E., 1990. Pre-Mesozoic Geology of Iberia. Springer, New
936 York.
937
938 Debrenne, F., 2007. Lower Cambrian archaeocyathan bioconstructions. Comptes Rendus Palevol
939 6, 5–19.
940
941 Derry, L.A., 2010. A burial diagenesis origin for the Ediacaran Shuram-Wonoka carbon isotope
942 anomaly. Earth and Planetary Science Letters 294, 152–162.
943
944 Dornbos, S.Q., Bottjer, D.J., 2000. Evolutionary paleoecology of the earliest echinoderms:
945 Helicoplacoids and the Cambrian substrate revolution. Geology 28, 839–842.
946
947 Eguiluz, L., Gil Ibarguchi, J.I., Ábalos, B., Apraiz, A., 2000. Superposed Hercynian and
948 Cadomian orogenic cycles in the Ossa-Morena Zone and related areas of the Iberian Massif.
949 Geological Society American Bulletin, 112: 1398-1413.
950
951 Erwin, D.H., Laflamme, M. Tweedt, S.M., Sperling, E.A., Pisani, D., Peterson. K.J., 2011. The
952 Cambrian conundrum: early divergence and later ecological success in the early history of
953 animals. Science 334, 109–1097.
954
955 Fedonkin, M., Liñán, E., Perejón, A., 1983. Icnofósiles de las rocas precámbrico-cámbricas de la
956 Sierra de Córdoba, España. Boletín de la Real Sociedad Española de Historia Natural, Geología
957 81(1–2), 125–138.

Feldmann, M., McKenzie, J., 1998. Stromatolite-thrombolite associations in a modern environment, Lee Stocking Island, Bahamas. Palaios 13, 201–212.

Fernández-Remolar, D.C., 1996. Los microfósiles problemáticos del Cámbrico Inferior de la Sierra de Córdoba: datos preliminares. Coloquios de Paleontología 48, 161–173.

Fernández-Remolar, D.C., 1998. Estudio paleontológico de taxones problemáticos del Cámbrico de Sierra Morena. Tesis Doctoral. Universidad Complutense de Madrid. Departamento de Paleontología. Madrid, Universidad Complutense de Madrid, pp. 306.

Fernández-Remolar, D.C., 1999. Las calizas fosforíticas del Ovetiense Inferior de la Sierra de Córdoba, España. Boletín de la Real Sociedad Española de Historia Natural (Sección Geológica) 95(1–4), 15–45.

Fernández-Remolar, D.C., 2001. Chancelloridae del Ovetiense Inferior de la Sierra de Córdoba, España. Revista Española de Paleontología 16(1), 39–61.

Fernández-Remolar, D.C., 2002. First record of Tannuolina Fonin & Smirnova, 1967 (Tomotiida) from the lower cambrian pedroche formation, southern spain. Revista Española de Micropaleontología 34(1), 39–51.

Flügel, E., 2004. Microfacies of carbonate rocks: Analysis, Interpretation, and Application.

981 Springer, New York.
982
983 Gozalo, R., Liñán, E., Palacios, T., Gámez-Vintaned, J.A., Mayoral, E., 2003. The Cambrian of
984 the Iberian Peninsula: An overview. Geologica Acta 1(1), 103–112.
985
986 Grotzinger, J.P., 1989. Facies and evolution of Precambrian carbonate depositional systems:
987 emergence of the modern platform archetype. Society of Economic Paleontologists and
988 Mineralogists Special Publication 44, 79–106.
989
990 Grotzinger, J.P., 1990. Geochemical model for Proterozoic stromatolite decline. American
991 Journal of Science 290A, 80–103.
992
993 Grotzinger, J.P., Knoll, A.H., 1999. Stromatolites in Precambrian carbonates: Evolutionary
994 mileposts or environmental dipsticks?. Annual Review of Earth and Planetary Sciences 27, 313–
995 358.
996
997 Grotzinger, J.P., James, N.P. 2000. Precambrian carbonates: Evolution of understanding. Society
998 for Sedimentary Geology (SEPM) Special Publication 67, 3–22.
999
1000 Grotzinger, J.P., Watters, W.A., Knoll, A.H., 2000. Calcified metazoans in thrombolite-
1001 stromatolite reefs of the terminal Proterozoic Nama Group, Namibia. Paleobiology 26, 334–359.
1002

1003 Gubanov, A.P., Fernández-Remolar, D.C., Peel, J.S., 2004. Early Cambrian molluscs from Sierra
1004 de Córdoba (Spain). Geobios 37, 199–215.
1005
1006 Hernández Pacheco, E., 1907. Los martillos de piedra y las piedras con cazoletas de las antiguas
1007 minas de cobre de la Sierra de Córdoba. Boletín de la Real Sociedad Española de Historia
1008 Natural 7, 279–292.
1009
1010 Hernández Pacheco, E., 1917. La fauna primordial de la Sierra de Córdoba. Asociación Española
1011 para el Progreso de las Ciencias. Conferencias. Sección 4ª Ciencias Naturales, 76–85.
1012
1013 Hernández Pacheco, E., 1918a. Les Archaeocyathidae de la Sierra de Córdoba (Espagne).
1014 Compte Rendus des séances de l'Academie des Sciences 166, 691–693.
1015
1016 Hernández Pacheco, E., 1918b. Le Cambrien de la Sierra de Córdoba (Espagne). Compte Rendus
1017 des séances de l'Academie des Sciences 166, 611–613.
1018
1019 Hernández Pacheco, E., 1926. La Sierra Morena y la llanura Ibérica (Síntesis geológica). XIV
1020 Congreso Geológico Internacional, Instituto Geológico y Minero de España.
1021
1022 Hernández-Sampelayo, P., 1933. El Cambriano en España. Memoria XVI Congreso Geológico
1023 Internacional, Madrid, Instituto Geológico y Minero de España.
1024

1025 Hernández-Sampelayo, P., 1935. Explicación del nuevo mapa geológico de España: El Sistema
1026 Cambriano. Memoria del Instituto Geológico y Minero de España 1, 297–525.
1027
1028 Hicks, M., Rowland, S.M., 2009. Early Cambrian microbial reefs, archaeocyathan inter-reef
1029 communities, and associated facies of the Yangtze Platform. Palaeogeography,
1030 Palaeoclimatology, Palaeoecology 281, 137–153.
1031
1032 Hinz-Schallreuter, I., Gozalo, R., Liñán, E., 2008. New bradorid arthropods from the Lower
1033 Cambrian of Spain. Micropaleontology 53, 497–510.
1034
1035 Holland, S.M., 1995. The stratigraphic distribution of fossils. Paleobiology 21, 92–109.
1036
1037 Ingram, R.L., 1954. Terminology for the thickness of stratification and parting units in
1038 sedimentary rocks. Bulletin of the Geological Society of America 65, 937–938.
1039
1040 James, N.P., Debrenne, F., 1980. Lower Cambrian bioherms: pioneer reefs of the Phanerozoic.
1041 Acta Palaeontologica Polonica 25(3–3), 655–668.
1042
1043 Jensen, S., Palacios, T., Martí Mus, M., 2010. Revised biochronology of the Lower Cambrian on
1044 the Central Iberian zone, Iberian massif, Spain. Geological Magazine 147, 690–703.
1045

1046 Julivert, M., Fontboté, J. M., Ribeiro, A., Nabais-Conde, L. E., 1972. Mapa Tectónico de la
1047 Península Ibérica y Baleares a escala 1:1,000,000. Memoria explicativa [1974]. IGME, Madrid,
1048 113 pp.
1049
1050 Knauth, L.P., Kennedy, M.J., 2009. The late Precambrian greening of the Earth. Nature 460,
1051 728–732.
1052
1053 Knoll, A.H., Carroll, S.B., 1999. The early evolution of animals: Emerging views from
1054 comparative biology and geology. Science 284, 2129–2137.
1055
1056 Knoll, A.H., Swett, K., 1990. Carbonate deposition during the late Proterozoic Era: an example
1057 from Spitsbergen. American Journal of Science 290-A, 104–132.
1058
1059 Kouchinsky, A., Bengtson, S., Pavlov, V., Runnegar, B., Torssander, P., Young, E., Ziegler, K.,
1060 2007. Carbon isotope stratigraphy of the Precambrian–Cambrian Sukharikha River section,
1061 northwestern Siberian platform. Geological Magazine 144, 1–10.
1062
1063 Kouchinsky, A., Bengtson, S., Runnegar, B., Skovsted, C., Steiner, M., Vendrasco M., 2012.
1064 Chronology of early Cambrian biomineralization. Geological Magazine 149, 221–251.
1065
1066 Landing, E., Geyer, G., Brasier, M.D., Bowring, S.A., *in press*. Cambrian Evolutionary
1067 Radiation: Context, correlation, and chronostratigraphy—overcoming deficiencies of the first
1068 appearance datum (FAD) concept. Earth-Science Reviews.

Landing, E., Bowring, S.A., Davidek, K.L., Westrop, S.W., Geyer, G., Heldmaier, W., 1998. Duration of the Early Cambrian: U-Pb ages of volcanic ashes from Avalon and Gondwana. Canadian Journal of Earth Sciences 35, 329–338.

Liñán, E., 1974. Las formaciones cámbricas del norte de Córdoba. Acta Geológica Hispánica 9, 21–26.

Liñán, E., 1978. Bioestratigrafía de la Sierra de Córdoba. Tesis Doctoral, Universidad de Granada, Granada.

Liñán, E., Dabrio, C., 1974. Litoestratigrafía del tramo inferior de la Formación Pedroche (Cámbrico inferior, Córdoba). Acta Geológica Hispánica 9(1), 21–26.

Liñán, E., Gámez-Vintaned, J.A., 1993. Lower Cambrian paleogeography of the Iberian Peninsula and its relations with some neighbouring European areas. Bulletin de la Societé Géologique France 164(6), 831–842.

Liñán, E., Mergl, M., 1982. Lower Cambrian Brachiopods of Sierra Morena, SW Spain. Boletín de la Real Sociedad Española de Historia Natural, Sección Geológica 80, 207–220.

1090 Liñán, E., Palacios, T., 1983. Aportaciones micropaleontológicas para el conocimiento del límite
1091 Precámbrico-Cámbrico en la Sierra de Córdoba, España. Comunicações dos Serviços Geológicos
1092 de Portugal 69(2), 227–234.
1093
1094 Liñán, E., Quesada, C., 1990. Rift Phase (Cambrian), in: Dallmeyer, R.D., Martínez García, E.
1095 (Eds.), Pre-Mesozoic Geology of Iberia. Springer, New York, pp. 259–266.
1096
1097 Liñán, E., Sdzuy, K., 1978. A trilobite from the Lower Cambrian of Córdoba (Spain) and its
1098 stratigraphical significance. Senckenbergiana Lethaea 59(4/5), 387–399.
1099
1100 Liñán, E., Álvaro, J., Gozalo, R., Gámez-Vintáned, J.A., Palacios, T., 1995. El Cámbrico Medio
1101 de la Sierra de Córdoba (Ossa-Morena, S de España): trilobites y paleoicnología. Implicaciones
1102 bioestratigráficas y paleoambientales. Revista Española de Paleontología 10(2), 219–238.
1103
1104 Liñán, E., Dies, M.E., Gámez Vintaned, J.A., Gozalo, R., Mayoral, E., Muñiz, F., 2005. Lower
1105 Ovetian (Lower Cambrian) trilobites and biostratigraphy of the Pedroche Formation (Sierra de
1106 Córdoba, southern Spain). Geobios 38, 365–381.
1107
1108 Liñán, E., Gonçalves, F., Gámez Vintaned, J. A., Gozalo, R., 1997. Evolución paleogeográfica
1109 del Cámbrico de la Zona de Ossa-Morena basada en el registro fósil, in: Araújo, A. A., Pereira
1110 Évora, M. F. (Eds.), Estudo sobre a Geologia da Zona de Ossa-Morena (Maciço Ibérico), Livro
1111 de Homenagem a Professor Francisco Gonçalves. Universidad de Évora, pp. 1–26.

1112 Liñán, E., Gozalo, R., Dies Álvarez, M.E., Gámez Vintaned, J.A., Zamora, S., 2008. Nuevos
1113 trilobites del Ovetiense inferior (Cámbrico Inferior bajo) de Sierra Morena (España).
1114 Ameghiniana 45, 123–128.
1115
1116 Liñán, E., Moreno-Eiris, E., Perejón, A., Schmitt, M., 1981. Fossils from the basals levels of the
1117 Pedroche Formation, Lower Cambrian (Sierra Morena, Córdoba, Spain). Boletín de la Real
1118 Sociedad Española de Historia Natural, Sección Geológica 79, 277–286.
1119
1120 Liñán, E., Perejón, A., Sdzuy, K., 1993. The Lower-Middle Cambrian stages and stratotypes
1121 from the Iberian Peninsula: a revision. Geological Magazine 130, 817–833.
1122
1123 Lotze, F., 1945. Zur Gliederung der Variszíden der Iberischen Meseta. Geotektonische
1124 Forschungen 6, 78–92.
1125
1126 Maloof, A.C., Schrag, D.P., Crowley, J.L., Bowring, S.A., 2005. An expanded record of Early
1127 Cambrian carbon cycling from the Anti-Altas Margin, Morocco. Canadian Journal of Earth
1128 Sciences 42, 2195–2216.
1129
1130 Maloof, A.C., Porter, S.M., Moore, J.L., Dudás, F.Ö., Bowring, S.A., Higgins, J.A., Fike, D.A.,
1131 Eddy, M.P., 2010a. The earliest Cambrian record of animals and ocean geochemical change.
1132 Geological Society of America Bulletin 122, 1731–1774.
1133

1134 Maloof, A.C., Ramezani, J., Bowring, S.A., Fike, D.A., Porter, S.M., Mazouad, M., 2010b.
1135 Constraints on early Cambrian carbon cycling from the duration of the Nemakit-Daldynian–
1136 Tommotian boundary $\delta^{13}C$ shift, Morocco. Geology 38, 623–626.
1137
1138 Matte, P., 1991. Accretionary history and crustal evolution of the Variscan belt in Western
1139 Europe. Tectonophysics 196: 309–337.
1140
1141 Menéndez, S., Moreno-Eiris, E., Perejón, A., 1999. Los arqueociatos y las facies carbonatadas de
1142 Cámbrico Inferior del Arroyo Guadalbarbo, Córdoba, España. Boletín de la Real Sociedad de
1143 Historia Natural, Sección Geológica 94(3–4), 63–91.
1144
1145 Moreno-Eiris, E., 1987a. Los montículos arrecifales de Algas y Arqueociatos del Cámbrico
1146 inferior de Sierra Morena I: Estratigrafía y facies. Boletín Geológico Minero 98(3): 295–317.
1147
1148 Moreno-Eiris, E., 1987b. Los montículos arrecifales de Algas y Arqueociatos del Cámbrico
1149 inferior de Sierra Morena II: Las algas calcáreas. Boletín Geológico Minero 98(4): 449–459.
1150
1151 Moreno-Eiris, E., 1987c. Los montículos arrecifales de Algas y Arqueociatos del Cámbrico
1152 inferior de Sierra Morena III: Microfacies y Diagénesis. Boletín Geológico Minero 98(5): 591–
1153 621.
1154

1155 Moreno-Eiris, E., 1987. Los montículos arrecifales de Algas y Arqueociatos del Cámbrico
1156 inferior de Sierra Morena IV: Bioestratigrafía y Sistemática de los Arqueociatos. Boletín
1157 Geológico Minero 98(6), 729–779.
1158
1159 Moreno-Eiris, E., Perejón, A., Rodríguez, S., Falces, S., 1995. Paleozoic Cnidaria and Porífera
1160 from Sierra Morena. VII International Symposium on Fossil Cnidaria and Porífera, 16–22
1161 September, 1995 Field Trip D, Madrid.
1162
1163 Myrow, P.M., Taylor, J.F., Runkel, A.C., Ripperdan, R.L., 2012. Mixed siliciclastic-carbonate
1164 upward-deepening cycles of the upper Cambrian inner detrital belt of Laurentia. Journal of
1165 Sedimentary Research 82, 216–231.
1166
1167 Payne, J.L., Lehrmann, D.J., Wei, J., Knoll, A.H., 2006. The pattern and timing of biotic
1168 recovery from the end-Permian mass extinction on the Great Bank of Guizhou, Guizhou
1169 Province, south China. Palaios 20, 63–85.
1170
1171 Peng, S., Babcock, L.E., 2011. Continuing progress on chronostratigraphic subdivision of the
1172 Cambrian System. Bulletin of Geosciences 86, 391–396.
1173
1174 Perejón, A., 1971. Pachecocyathus, nuevo género de Archaeocyathidos del Cámbrico español.
1175 Estudios Geológicos 4, 143–149.
1176

1177 Perejón, A., 1975a. Nuevas Faunas de Arqueociatos del Cámbrico Inferior de Sierra Morena (I).
1178 Tecniterrae 8, 8–29.
1179
1180 Perejón, A., 1975b. Arqueociatos de los subórdenes Monocyathina y Dokidocyathina. Boletín de
1181 la Real Sociedad de Historia Natural, Sección Geológica 73(1–4), 125–145.
1182
1183 Perejón, A., 1975c. Arqueociatos Regulares del Cámbrico Inferior de Sierra Morena (SW de
1184 España). Boletín de la Real Sociedad de Historia Natural, Sección Geológica 73(1–4), 147–193.
1185
1186 Perejón, A., 1976a. Nuevas Faunas de Arqueociatos del Cámbrico Inferior de Sierra Morena (II).
1187 Tecniterrae 9, 7–24.
1188
1189 Perejón, A., 1976b. Nuevos datos sobre los Arqueociatos de Sierra Morena. Estudios Geológicos
1190 32(1), 5–33.
1191
1192 Perejón, A., 1977. Arqueociatos con túmulos en el Cámbrico Inferior de Córdoba (Sierra Morena
1193 Oriental). Estudios Geológicos 33(6), 545–555.
1194
1195 Perejón, A., 1986. Bioestratigrafía de los Arqueociatos en España. Cuadernos de Geología
1196 Ibérica 9, 213–216.
1197

1198 Perejón, A., 1989. Arqueociatos del Ovetiense en las sección del Arroyo Pedroche, Sierra de
1199 Córdoba, España. Boletín de la Real Sociedad Española de Historia Natural (Geología) 84, 143–
1200 247.
1201
1202 Perejón, A., 1994. Palaeogeographic and biostratigraphic distribution of Archaeocyatha in Spain.
1203 Courier Forschungsinstitut Senckenberg 172, 341–354.
1204
1205 Perejón, A., Moreno-Eiris, E., 2006. Biostratigraphy and paleobiogeography of the
1206 archaeocyaths on the south-western margin of Gondwana. Zeitschrift der deutschen Gesellschaft
1207 für Geowissenschaften 157(4), 611–627.
1208
1209 Perejón, A. Moreno-Eiris, E., 2007. Ovetian cryptic archaeocyaths, lower Cambrian from Las
1210 Ermitas (Córdoba, Spain), in: Hubmann, B., Piller, W.E., (Eds.), Fossil Corals and Sponges.
1211 Proceedings of the 9th International Symposium on Fossil Cnidaria and Porifera. Austrian
1212 Academy of Sciences, Schriftenreihe der Erdwissenschaftlichen Kommission 17, pp. 113–137.
1213
1214 Perejón, A., Moreno-Eiris, E., Liñán, E., Sequeiros, L., 1996. The Cambrian of the Sierra de
1215 Córdoba. (Ossa- Morena Zone. Sierra Morena), in: Liñán E., Gozalo, R. (Eds.), II Field
1216 Conference of the Cambrian stage subdivision working groups. Internacional Subcomission on
1217 Cambrian stratigraphy. Spain, 13-21 Sept. 1996. Field Trip Guide and Abstracts, 45–55.
1218
1219 Pérez-Estaún, A., Bea, F., 2004. Macizo Ibérico, in: Vera, J.A. (Ed.), Geología de España.
1220 Sociedad Geológica de España e Instituto Geológico de España, pp. 21–230.

1221

1222 Peterson, K.J., Lyons, J.B., Nowak, K.S., Takacs, C.M., Wargo, M.J., McPeek, M.A., 2004.
1223 Estimating metazoan divergence times with a molecular clock. Proceedings of the National
1224 Academy of Sciences 101, 6536–6541.

1225

1226 Pratt, B.R., 1984. *Epiphyton* and *Renalcis* – Diagenetic microfossils from calcification of
1227 coccoid blue-green algae. Journal of Sedimentary Petrology 54, 948–971.

1228

1229 Pratt, B.R., James, N.P., 1982. Cryptalgal-metazoan bioherms of Early Ordovician age in the St-
1230 George Group, Western Newfoundland. Sedimentology 29, 543–569.

1231

1232 Pratt, B.R., James, N.P., 1986. The St. George Group (Lower Ordovician) in western
1233 Newfoundland: tidal flat island model for carbonate sedimentation in shallow epeiric Seas.
1234 Sedimentology 33, 313–343.

1235

1236 Pruss, S.A., Finnegan, S., Fischer, W.W., Knoll, A.H., 2010. Carbonates in skeleton-poor seas:
1237 New insights from Cambrian and Ordovician strata of Laurentia. Palaios 25, 73–84.

1238

1239 Pruss, S.A., Clemente, H., 2011. Assessing the role of skeletons in Early Paleozoic carbonate
1240 production: Insights from Cambro-Ordovician strata, Western Newfoundland, in: Laflamme, M.,
1241 Schiffbauer, J.D., Dornbos, S.Q. (Eds.), Quantifying the Evolution of Early Life, Numerical
1242 approaches to the evaluation of fossils and ancient ecosystems. Springer, New York, pp. 161–
1243 183.

Pruss, S.A., Clemente, H., Laflamme, M., 2012. Early (Series 2) Cambrian archaeocyathan reefs of southern Labrador as a locus for skeletal carbonate production. Lethaia 45, 401–410.

Quesada, C., 1990, Precambrian sucessions in SW Iberia: their relationship to "Cadomian" orogenic events, in: D'Lemos, D. S., Strachman, R. A., Topley, C. G. (Eds.), The Cadomian Orogeny. Geological Society Special Publication 51, pp. 353–362.

Rodríguez-Martínez, M., Heim, C., Quéric, N.-V., Reitner, J., 2011, Frutexites, in: Reitner, J., Thiel, V. (Eds.), Encyclopedia of Geobiology, Springer, New York, pp. 396-401.

Rowland, S.M., Gangloff, R.A., 1988. Structure and paleoecology of Lower Cambrian reefs. Palaios 3, 111–135.

Rozanov, A.Yu, Parkhaev, P.Yu., Demidenko, Yu., Skorlotova, N.A., 2011. *Mobergella radiolata*—a possible candidate for defining the base of Cambrian Series 2 and Stage 3. Museum of Northern Arizona Bulletin 67, 304–306.

Sarmiento, J.L. Gruber, N., 2006. Ocean biogeochemical dynamics. Princeton University Press, New Jersey.

1265 Schmitt, M., 1982. Columnar stromatolites from the Lower Cambrian Formation Pedroche,
1266 Sierra Morena, S. Spain. Boletín de la Real Sociedad Española de Historia Natural, Sección
1267 Geológica 80(1–4), 5–23.
1268
1269 Shapiro, R.S., 2000. A comment on the systematic confusion on thrombolites. Palaios 15, 166–
1270 169.
1271
1272 Simon, W., 1939. Archaeocyathea: I. Kritischie Sitchung der Spuer Familie. II. Die Fauna im
1273 Kambrim der Sierra Morena (Spanien). Abhandlungen Senckenbergischen Naturforshenden
1274 Gessellschaft 448, 1–87.
1275
1276 Smith, A.B., 1985. Cambrian eleutherozoan echinoderms and the early diversification of
1277 edrioasteroids. Palaeontology 28, 715–756.
1278
1279 Steiner, M., Li, G., Ergaliev, G., 2011. Toward a subdivision of the traditional Lower Cambrian.
1280 Museum of Northern Arizona Bulletin 67, 306–308.
1281
1282 Thomas, R.D.K., Shearman, R.M., Stewart, C.W., 2000. Evolutionary exploitation of design
1283 options by the first animals with hard skeletons. Science 288, 1239–1242.
1284
1285 Van der Plas, L., Tobi, A.C., 1965. A chart for judging the reliability of point counting results.
1286 American Journal of Science 263, 87–90.
1287

1288 Vennin, E., Álvaro, J.J., Moreno-Eiris, E., Perejón, A., 2003. Early Cambrian coelobiontic
1289 communities in tectonically unstable crevices developed in Neoproterozoic andesites, Ossa-
1290 Morena, southern Spain. Lethaia 36, 53–65.
1291
1292 Zamarreño, I., 1977. Early Cambrian Algal Carbonates in Southern Spain, in: Flügel, E. (Ed.),
1293 Fossil Algae: Recent Results and Developments. Springer-Verlag, Berlín, pp. 360–365.
1294
1295 Zamarreño, I, Debrenne, F., 1977. Sédimentologie et biologie des constructions organogénes du
1296 Cambrien inféreur du Sud de l'Espagne. Mémoires du Bureau de Recherches Géologiques et
1297 Miniéres 89, 49–61.
1298
1299 Zeebe, R.E., Westbroek, P., 2003. A simple model for the $CaCO_3$ saturation state of the ocean:
1300 The "Strangelove", the "Neritan", and the "Cretan" Ocean. Geochemistry, Geophysics,
1301 Geosystems 4, 1104, doi:10.1029/2003GC000538.
1302
1303 Zhu, M.Y., Babcock, L.E., Peng, S.C., 2006. Advances in Cambrian stratigraphy and
1304 paleontology: integrating correlation techniques, paleobiology, taphonomy and
1305 paleoenvironmental reconstruction. Palaeoworld 15, 217–222.

FIGURE 1—Geology and map of the study area. A) Google Earth image with locations (white dots) of the three measured stratigraphic sections near the city of Córdoba, Spain. B) Generalized Neoproterozoic to Cambrian stratigraphy of the Ossa Morena Zone, Iberian massif (adapted from Gubanov et al., 2004).

FIGURE 2—Lithostratigraphy and $\delta^{13}C_{carb}$ chemostratigraphy of the Pedroche Formation. LE = Cerro de Las Ermitas section; PR = Pilgrimage Road section; AP = Arroyo Pedroche section. Samples of lithologies point-counted for percent constituent components are denoted with a small arrow next to the stratigraphic height. PR and AP $\delta^{13}C_{carb}$ chemostratigraphy are plotted as 3-pt running averages. Thrombolite megastructure (facies A-0 through A-V; see Section 5.1.1), nodular limestone (facies B; see Section 5.1.1), ooid/oncoid/peloid grainstone (facies C; see Section 5.1.2) and silt-bearing mixed carbonate mudstone/wackestone and packstone/floatstone/rudstone (facies D; see Section 5.1.3) are illustrated in Figure 4.

FIGURE 3—Lithologic character of the thrombolite lithofacies. A) Isolated, bioherm (A-III) surrounded by bedded carbonate and siliciclastics (AP 49.0 m). The dashed line delineates the contact between the thrombolite bioherm and onlapping siltstone beds. B) Columnar heads separated by siliciclastic siltstone (the dashed line outlines one columnar thrombolite head). C) Thrombolite biostrome with interbeds and irregular drapes and pockets of siltstone. D) Archaeocyath clasts within a thrombolitic bed.

FIGURE 4—Schematic of Pedroche Formation lithofacies. Facies A: Calcimicrobial thrombolite (see Figs. 3 and 5a,b). See Section 5.1.1 for descriptions of isolated (A-0), biohermal

(A-I, A-II, and A-III), and biostromal (A-IV and A-V) megastructures and the figure inset for a key to the mesoclot textures that comprise the internal mesostructure of thrombolite megastructures (mesostructures a – j). Facies B: Nodular limestone that surrounds calcimicrobial thrombolite bioherms (A-I and A-II) and displays a mottled texture imparted by thrombolitic mesoclots. Facies C: Massive lenses (facies C1); small, channelized lithosomes (C2); and planar cross-bedded tabular beds (C3) of ooid, oncoid and peloid grainstone. Facies assemblage D: interbedded massive carbonate mudstone, bioclastic wackestone, archaeocyathan packstone–floatstone–rudstone and siliciclastic siltstone (see Figs. 8a,b,c and 9a). These lithologies grade into and out of one another over a sub-cm spatial scale, thus we do not subdivide this facies into individual lithologic components.

FIGURE 5—Photomicrographs of the modes of fossil preservation within the Arroyo Pedroche and Pilgrimage Road sections. (Photomicrographs at 6.3x magnification.) A) Arboreal thrombolite mesoclot texture (AP 49.5 m). B) Epiphyton comprising a thrombolite mesoclot (AP 49.5 m). C) Dolomitized trilobite carapace (width = 6 mm; AP 92.6 m). D) Calcitic brachiopod (AP 92.6 m). E) Small shelly fossil (AP 61.0 m).

FIGURE 6—Lithologic character of the ooid/oncoid/peloid grainstone lithofacies. A) Fine-grained, well-sorted ooid grainstone (AP 61 m). B) Poorly-sorted ooid/oncoid/peloid grainstone (scale bar = 1 cm).

FIGURE 7—Photomicrographs of the ooid/oncoid/peloid grainstone lithofacies taken at 6.3x magnification. An ooid replaced by dolomite rhombs (oomold) in A) plane-polarized light (AP

92.6 m) and B) cross-polarized light (AP 92.6 m). C) A peloid replaced by ferroan dolomite rhombs (AP 17.0 m). D) An ooid with a micritic cortoid fabric (AP 61.0 m). E) An ooid with a micritic cortoid fabric retaining a faint radial arrangement of neomorphosed crystals (AP 92.6 m). F) A nephroid peloid (AP 17.0 m).

FIGURE 8—Lithologic and petrographic character of the interbedded carbonate mudstone, bioclastic wackestone, archaeocyathan floatstone–packstone–rudstone and siliciclastic siltstone lithofacies (facies assemblage D) of the Cerro de Las Ermitas section. A) Outcrop appearance of this spatially-variable lithofacies (block pictured is located just above the measured stratigraphic section). B) Oriented bioclasts within an archaeocyathan rudstone. Rudstone facies common from LE 33.5 – 50 m. C) Photomicrograph of archaeocyathan boundstone with *Archaeopharetra* (Zones I-III; scale bar = 4 mm; sample LE 31.5 m). Photomicrographs of D) the silty microspar, mcr1, E) the drusy microspar, mcr2 and F) the late-stage sparry cement 'sp' (described in Section 5.1.3; all from sample LE 18.0 m).

FIGURE 9—Photomicrographs of archaeocyath-bearing lithofacies showing modes of archaeocyath preservation. A) Thin-section LE 18.0 m with text and arrows labeling relevant textures and features. SSF = small shelly fossil. B) An archaeocyath (*Nochoroicyathus)* with a silty microspar (mcr1) infilling the central cavity and intervallum (LE 48.0 m), a drusy microspar (mcr2) molding the walls, and an oncolitic halo surrounding the skeleton. C) An archaeocyath with mcr1 infilling the central cavity and intervallum and both mcr2 and a coarse spar (sp) molding the intervallum and walls (LE 29.0 m). D) An archaeocyath (family Ajacicyathidae)

with mcr2 molding the inner walls and sp infilling the central cavity and intervallum (LE 18.0 m). Scale bars represent 5, 0.5, 2 and 1 mm for frames A-D, respectively.

FIGURE 10—Modes of fossil preservation (exclusive of archaeocyaths) within the interbedded carbonate mudstone, bioclastic wackestone, archaeocyathan floatstone–packstone–rudstone and siliciclastic siltstone (lithofacies assemblage D). Photomicrographs (at 6.3x magnification) of A) a SSF from sample LE 18.0 m, B) a SSF from sample LE 33.0 m, and C) an unidentified bioclast from sample LE 48.0 m.

FIGURE 11—The percentage of skeletons within the Pedroche Formation as determined from point counts of representative petrographic thin-sections (see Table 2 for data). Individual circles represent data from a single thin section. The average value for each column is marked with a horizontal black line. A) Percent skeletal contribution by carbonate lithofacies. Samples representative of the carbonate mudstone (n = 5), bioclastic wackestone (n = 6), and archaeocyath rud./flts./pkst. (rudstone/floatstone/packstone; n = 5) lithofacies derive exclusively from section LE. Samples representative of thrombolite (n = 5) and oo./on./pel. (ooid/oncoid/peloid) grainstone lithofacies (n = 9) derive from sections AP and PR. B) Taxonomic identity of the skeletal contribution (i.e., archaeocyath versus small shelly fossil (SSF)) to the archaeocyathan rudstone/floatstone/packstone lithofacies and C) the bioclastic wackestone lithofacies.

FIGURE 12—The percent constituent components of the carbonate lithofacies of the Pedroche Formation as determined from point counts of representative petrographic thin-sections (see

Table 2 for data). Individual circles represent data from a single thin section. The average value for each column is marked with a horizontal black line. A) Constituent components of the bioclastic wackestone and archaeocyathan packstone–floatstone–rudstone lithofacies (facies assemblage D). B) Constituent components of the thrombolite lithofacies (facies A). C) Constituent components of the ooid/oncoid/peloid grainstone lithofacies (facies C).

FIGURE 13—A comparison of the percent skeletal contribution to archaeocyath-bearing reef and inter-reef lithologies of the Pedroche Formation and other reef/inter-reef localities. Individual circles represent data from a single thin section. The average value for each study is marked with a horizontal black line. A) Total skeletal contribution, B) archaeocyath skeletal contribution, and C) non-archaeocyath skeletal contribution to reef and inter-reef lithologies. D) The average percentage of archaeocyath (white) versus non-archaeocyath (black) skeletal material from the Pedroche Formation (this study), the Forteau Formation, southern Labrador (Pruss et al., 2012) and the Xiannudong Formation, southern China (Hicks and Rowland, 2009).

TABLE 1—The percent contribution of carbonate lithofacies (rows) to the total meterage of measured stratigraphic sections (columns) of the Pedroche Formation. (Carbonate-normalized percent contributions are reported in parentheses.)

TABLE 2—Raw point-count data from representative samples of the Cambrian Series 2, Stage 3 Pedroche Formation, Spain. Samples LE, AP, and PR were collected from the Cerro de Las Ermitas, Arroyo Pedroche, and Pilgrimage road section, respectively. Lithologic classification was determined by petrographic examination. Lithological abbreviations represent: Mdst =

mudstone, Wkst = wackestone, Grnst = grainstone, Rud = rudstone, and Th = thrombolite. Constituent component abbreviations represent: A. = archaeocyathan, Biocl. = bioclastic, Oo. = ooid, On. = oncoid, and Pel. = peloid. Numerical values in the table represent the abundance of identified components counted within a given thin-section. SSF = small shelly fossil.

TABLE 3—The average percent of constituent components (columns) within carbonate lithofacies (rows) of the Pedroche Formation.

Table 1

Sample	Lithology	Micrite	Spar	Siliciclastics & Stylocumulate	Vein	Ooid	Peloid	Archaeocyath	Trilobite	SSF	Clotted Micrite & Microbial	Other & Indistinguisable	Total Points
LE 16.5 m	Mdst	202	2	4	0	0	0	0	0	1	0	1	210
LE 18.0	A. Rud./Flts./Pkst.	114	27	11	6	0	0	20	0	12	19	1	210
LE 19.0	Mdst	169	7	3	9	0	0	0	0	1	0	0	189
LE 21.0	Mdst	197	0	11	1	0	0	1	0	3	0	0	213
LE 22.0 m	A. Wkst	84	94	19	0	0	0	10	0	0	0	5	212
LE 29.0 m (1)	Biocl. Wkst / A. Rud	122	6	33	0	0	0	22	0	12	0	3	198
LE 29.0 m (2)	Biocl. Wkst / A. Rud	132	1	32	0	0	0	12	0	4	0	0	181
LE 31.5 m	A. Rud./Flts./Pkst.	109	46	9	1	0	0	27	0	7	0	3	202
LE 32.0 m	A. Rud./Flts./Pkst.	149	9	31	0	0	0	1	0	11	0	4	205
LE 33.0 m	Biocl. Wkst	72	98	2	0	0	0	33	0	11	0	2	218
LE 35.0 m	Biocl. Wkst	153	0	20	2	0	0	1	0	9	0	5	190
LE 36.0 m	Biocl. Wkst / A. Rud	103	17	55	0	0	0	3	0	8	0	2	188
LE 40.0 m	Wkst / Mdst	160	4	11	2	0	0	1	0	6	0	5	189
LE 42.0 m	Mdst	204	9	0	2	0	0	0	0	2	0	0	217
LE 44.0 m	Mdst	152	2	20	0	0	0	0	0	0	0	0	174
LE 48.0 m	Biocl. / A. Wkst	160	23	2	1	0	0	1	0	8	1	2	198
AP 17.0 m	On. /Pel. Grnst	96	6	5	2	0	0	0	0	0	53	35	197
AP 18.0 m	Th	101	5	5	3	0	0	0	0	0	82	35	231
AP 49.0 m	Th	110	0	10	0	0	0	0	0	0	93	6	219
AP 49.5 m	Th	100	3	5	8	0	0	0	0	0	94	5	215
AP 61.0 m	Oo. / Pel. Grnst	65	4	7	9	68	0	0	0	0	28	5	186
AP 62.2 m	Th	128	0	8	0	0	0	0	0	0	72	10	218
AP 65.0 m	Th	97	0	36	1	0	0	0	0	0	69	17	220
AP 92.6 m	Oo. / Biocl. Grnst	87	2	25	0	51	5	0	4	0	5	2	181
PR 5.0 m	Oo. Grnst	62	4	4	2	112	0	0	0	0	0	2	186
PR 14.0 m	Oo. Grnst	125	3	0	1	77	0	0	0	0	0	6	212
PR 28.0 m	Pel. / Oo. Grnst	77	2	0	6	27	72	0	0	0	0	2	186
PR 30.0 m	Pel. / Oo. Grnst	64	51	4	0	20	66	0	0	0	0	5	210
PR 34.4 m	Pel. / Oo. Grnst	112	4	0	4	16	74	0	0	0	0	1	211
PR 77.5 m	Oo. Grnst	67	2	4	0	88	0	0	0	0	0	3	164

Table 2

Carbonate Lithofacies	Arroyo Pedroche	Pilgrimage Road	Las Ermitas
Calcimicrobial Thrombolite (facies A)	27% (60%)	26% (55%)	0%
Ooid/Oncoid/Peloid Grainstone (facies C)	3% (8%)	6% (13%)	0%
Inter-reef / Reef-flank Facies (facies assemblage D)	0%	0%	100%
Other Carbonate	14% (32%)	15% (31%)	0%

Table 3

Carbonate Lithofacies	Average % Skeletal	Average % Micrite	Average % Clotted Micrite / Microbial	Average % Ooids/Oncoids/Peloids
Calcimicrobial Thrombolite (facies A)	0	49.4	37.2	0
Ooid/Oncoid/Peloid Grainstone (facies C)	0.2	47.3	0	44.0
Inter-reef / Reef-flank Facies (facies assemblage D)	7.6	82.1	0.6	0

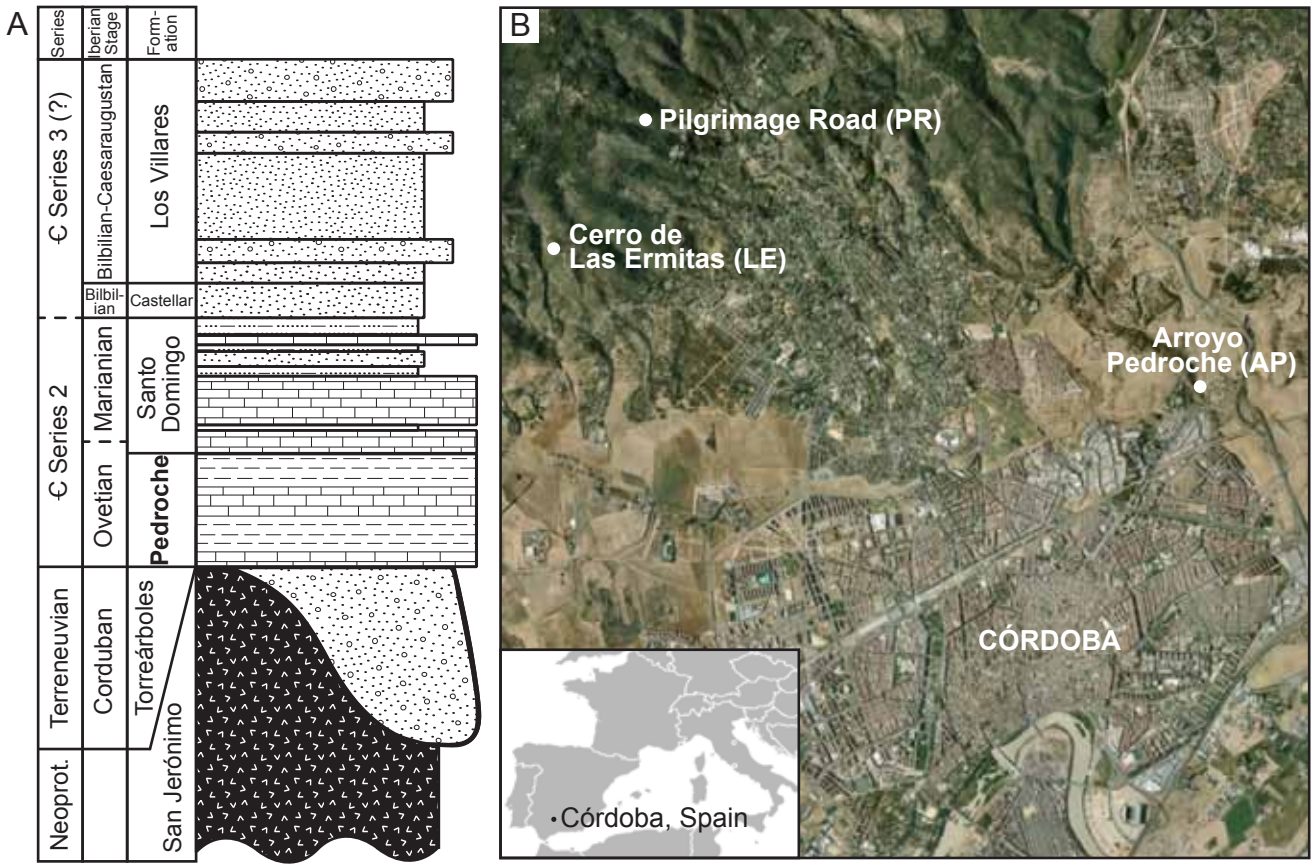
A
Series
Iberian Stage
Form-ation
Є Series 3 (?)
Bilbilian-Caesaraugustan
Los Villares
Bilbil-ian
Castellar
Є Series 2
Marianian
Santo Domingo
Ovetian
Pedroche
Terreneuvian
Corduban
Torreárboles
Neoprot.
San Jerónimo
B
Pilgrimage Road (PR)
Cerro de Las Ermitas (LE)
Arroyo Pedroche (AP)
CÓRDOBA
Córdoba, Spain

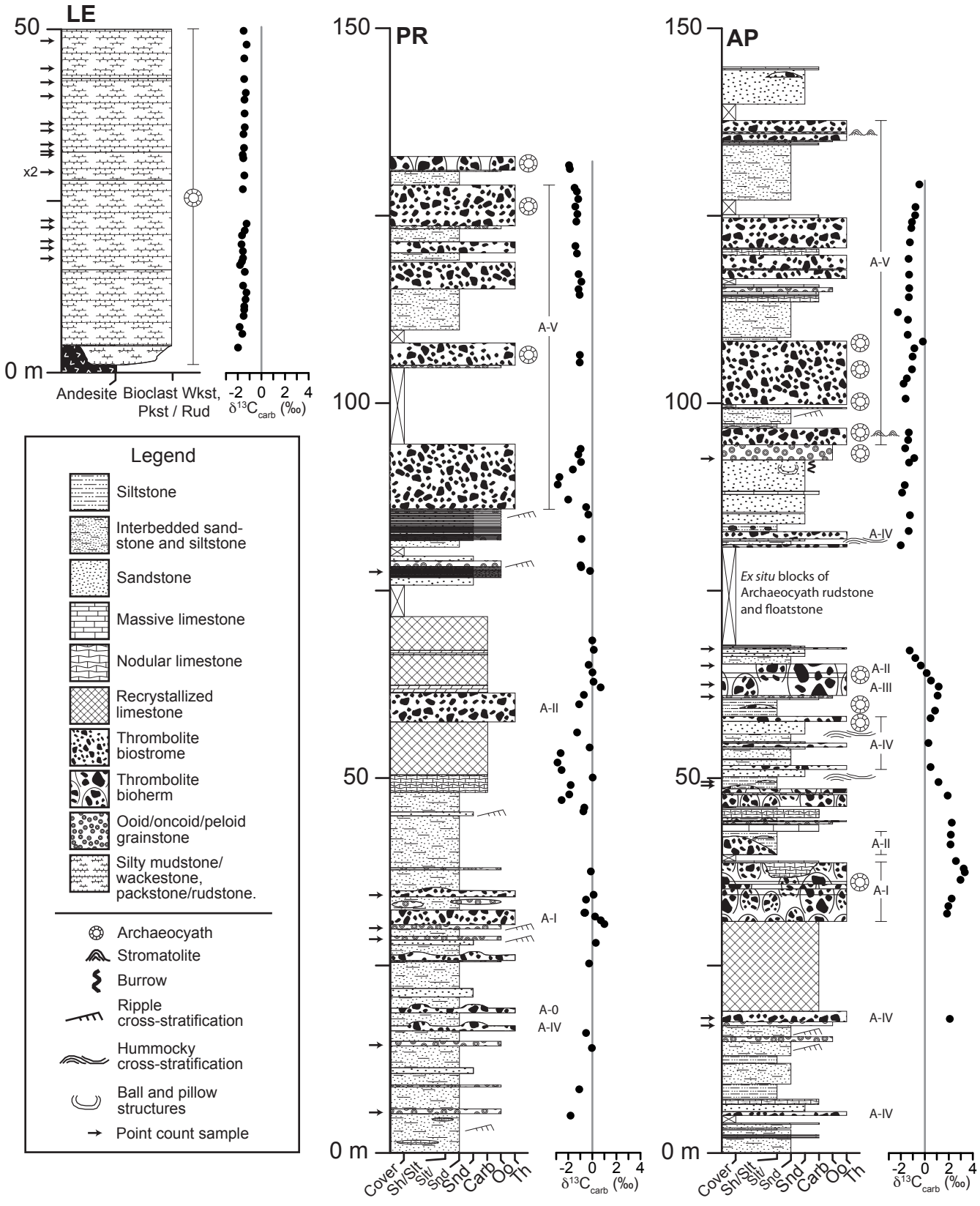
LE
50
x2
0 m
Andesite
Bioclast Wkst, Pkst / Rud
-2 0 2 4
δ13Ccarb (‰)
PR
150
100
50
0 m
A-V
A-II
A-I
A-0
A-IV
Cover
Sh/Slt
Slt/
Snd
Snd
Carb
Oo
Th
AP
150
100
50
0 m
A-V
A-IV
Ex situ blocks of Archaeocyath rudstone and floatstone
A-II
A-III
A-IV
A-II
A-I
A-IV
A-IV
Legend
Siltstone
Interbedded sand-stone and siltstone
Sandstone
Massive limestone
Nodular limestone
Recrystallized limestone
Thrombolite biostrome
Thrombolite bioherm
Ooid/oncoid/peloid grainstone
Silty mudstone/ wackestone, packstone/rudstone.
Archaeocyath
Stromatolite
Burrow
Ripple cross-stratification
Hummocky cross-stratification
Ball and pillow structures
Point count sample

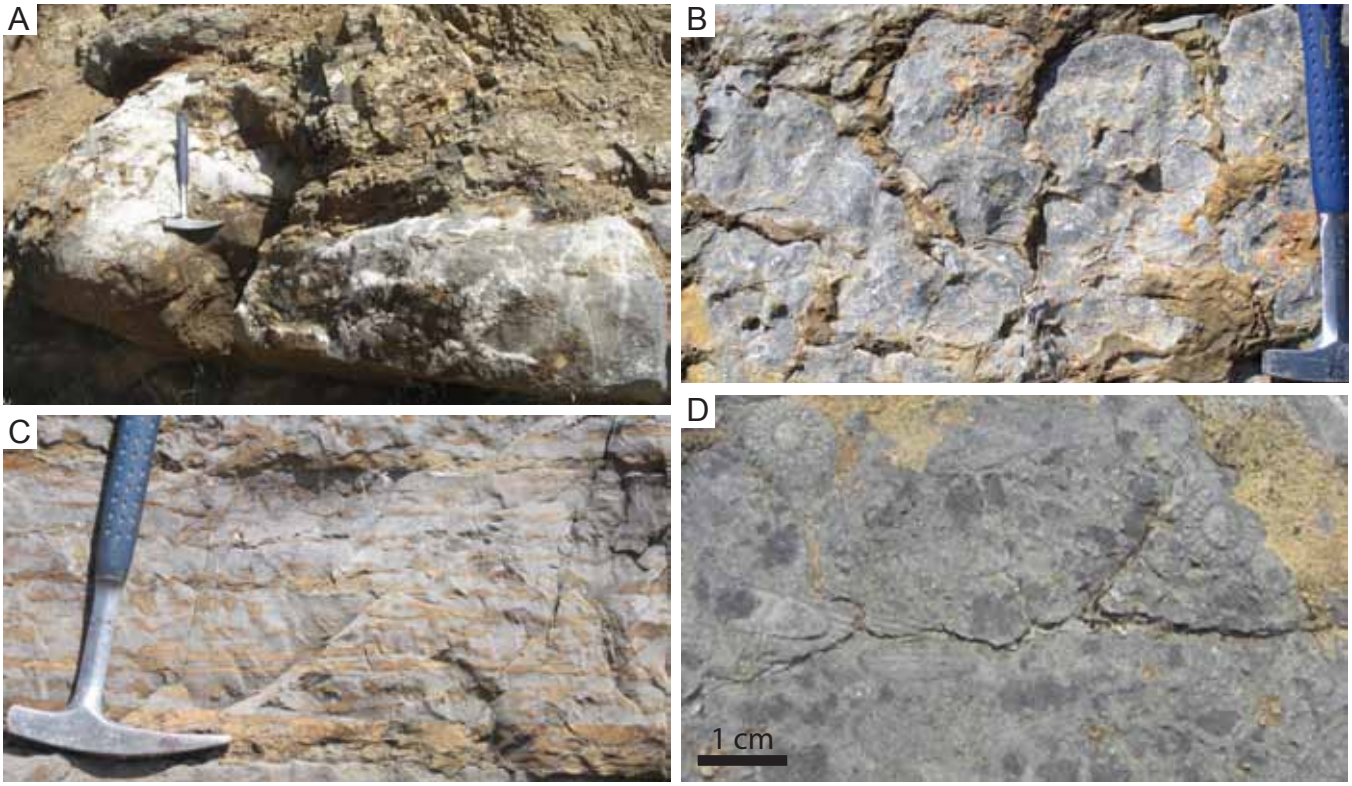
A
B
C
D
1 cm

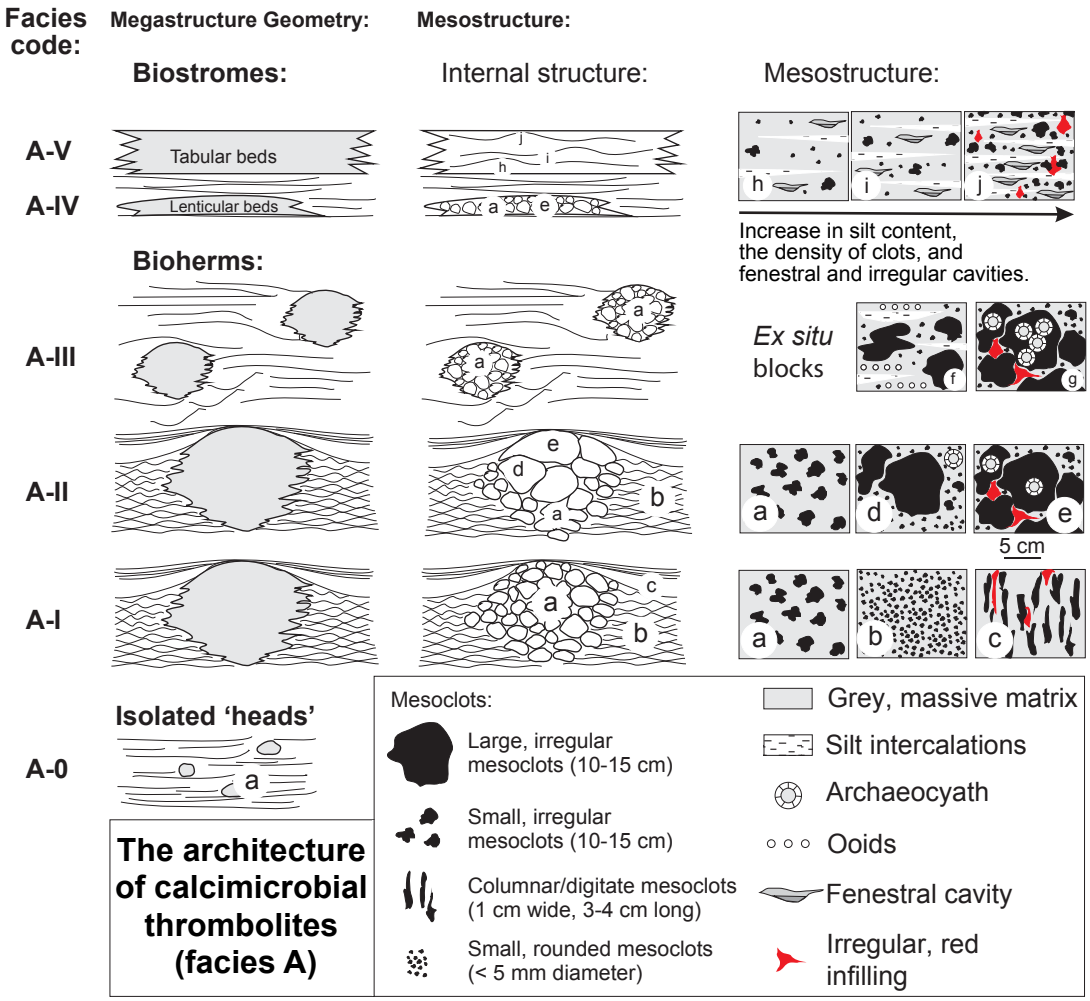
Facies code:
Megastructure Geometry:
Mesostructure:
Biostromes:
Internal structure:
Mesostructure:
A-V
A-IV
Tabular beds
Lenticular beds
Increase in silt content, the density of clots, and fenestral and irregular cavities.
Bioherms:
A-III
Ex situ blocks
A-II
5 cm
A-I
Isolated 'heads'
A-0
The architecture of calcimicrobial thrombolites (facies A)
Mesoclots:
Large, irregular mesoclots (10-15 cm)
Small, irregular mesoclots (10-15 cm)
Columnar/digitate mesoclots (1 cm wide, 3-4 cm long)
Small, rounded mesoclots (< 5 mm diameter)
Grey, massive matrix
Silt intercalations
Archaeocyath
Ooids
Fenestral cavity
Irregular, red infilling

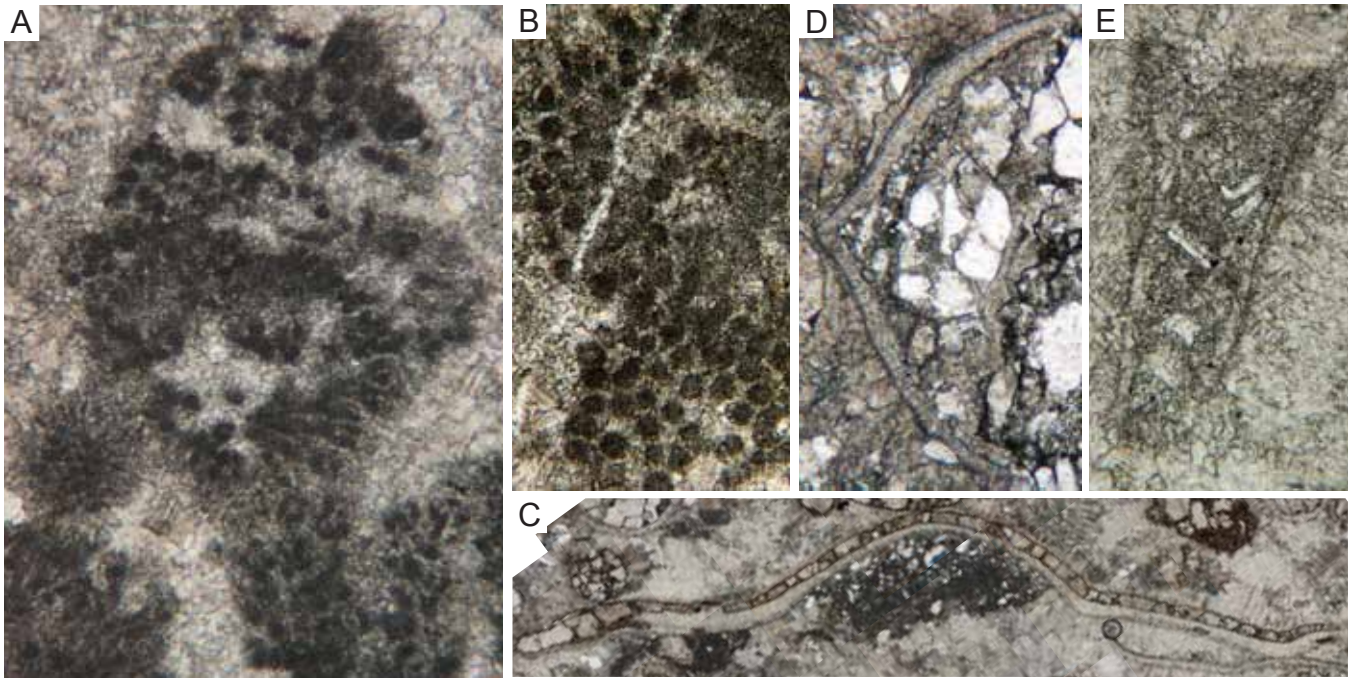
A
B
D
E
C

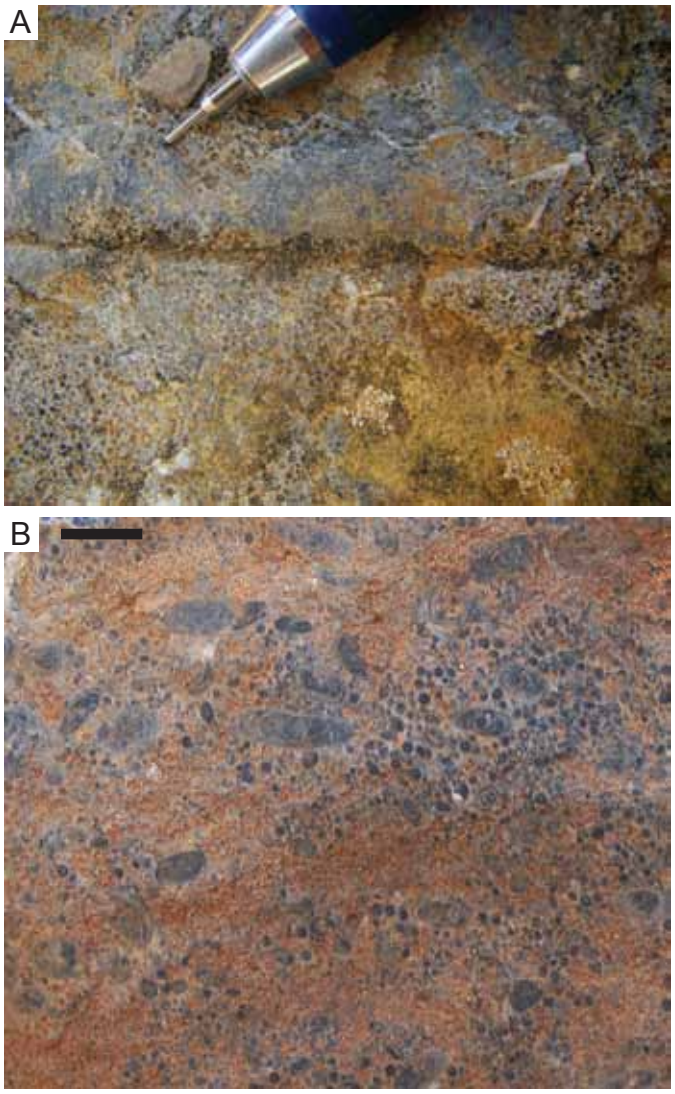
A
B

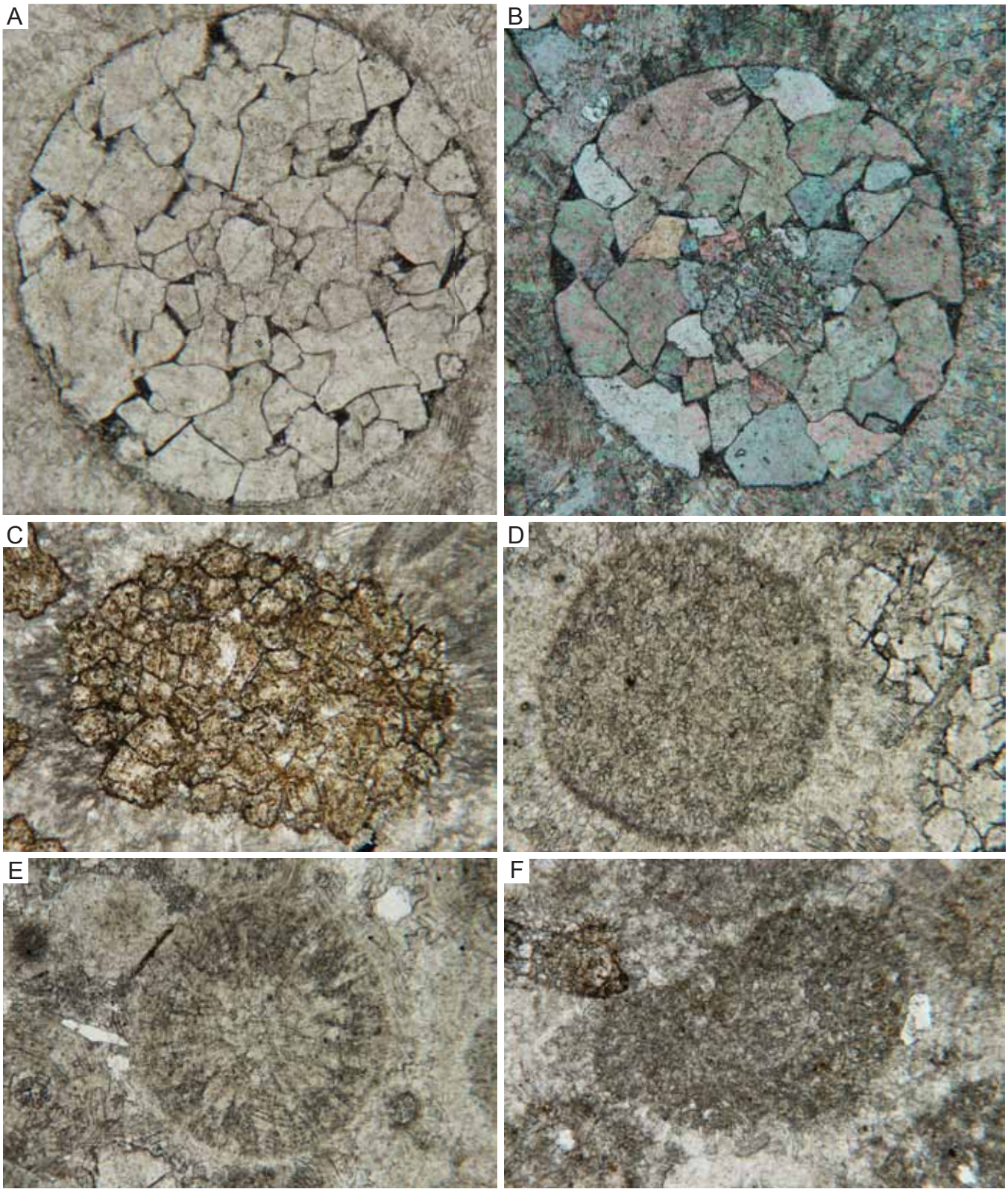
A
B
C
D
E
F

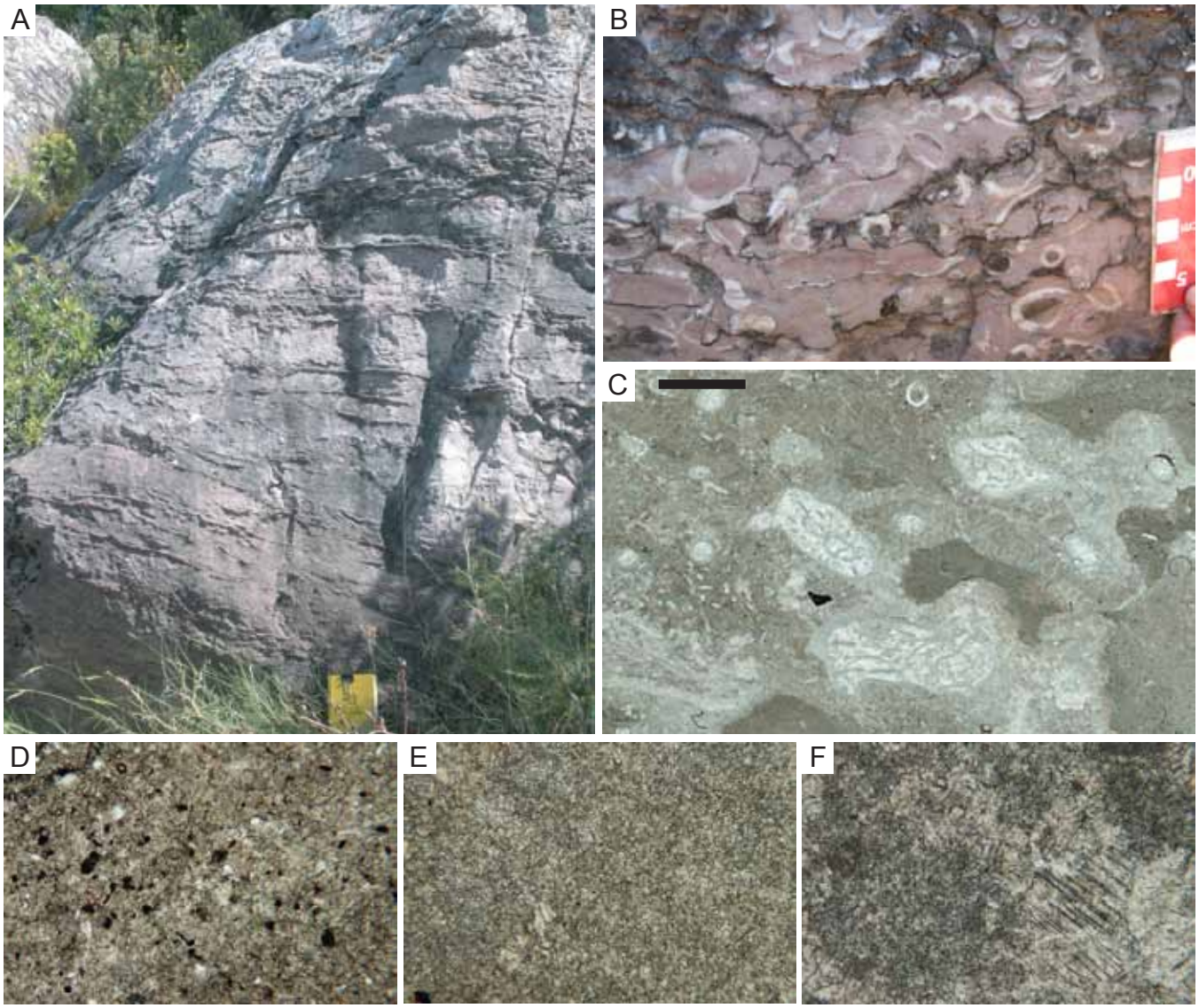
A
B
C
D
E
F

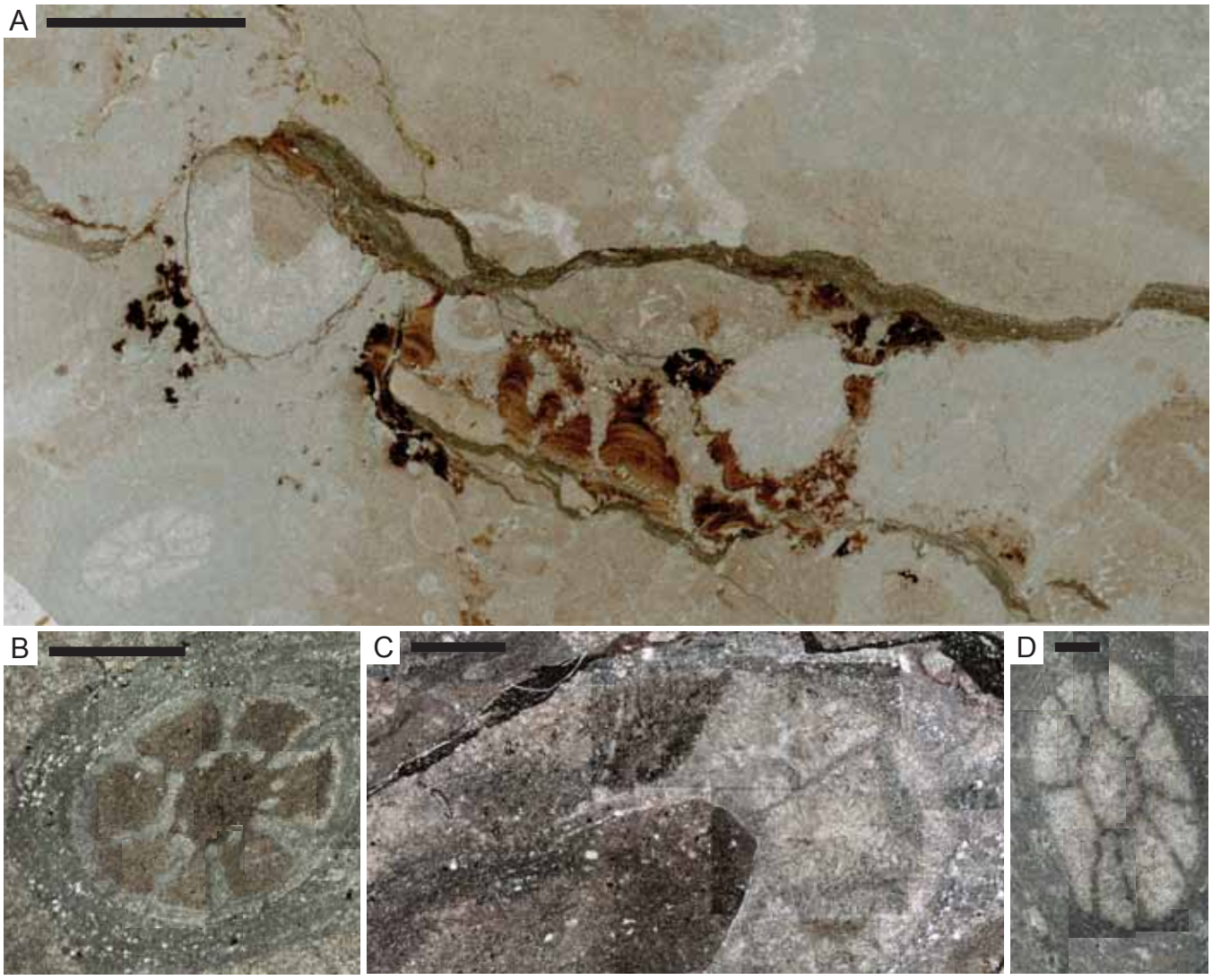
A
B
C
D

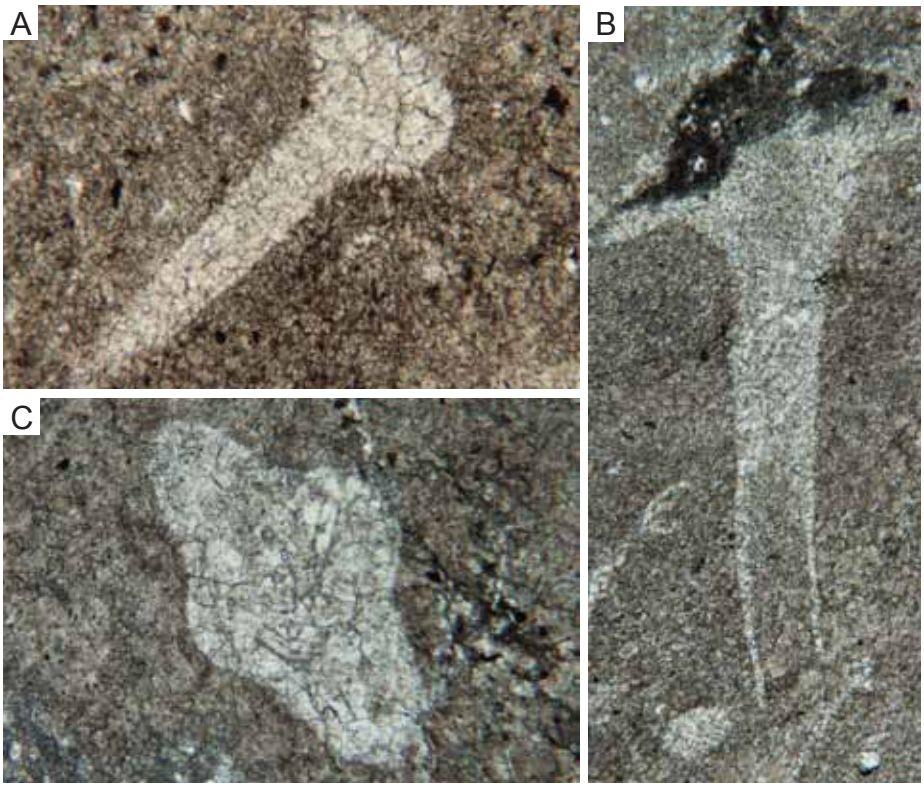
A
B
C

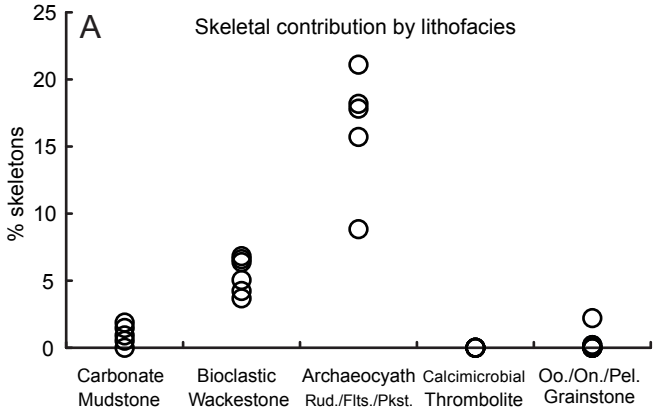
A
Skeletal contribution by lithofacies
% skeletons
25
20
15
10
5
0
Carbonate Mudstone
Bioclastic Wackestone
Archaeocyath Rud./Flts./Pkst.
Calcimicrobial Thrombolite
Oo./On./Pel. Grainstone

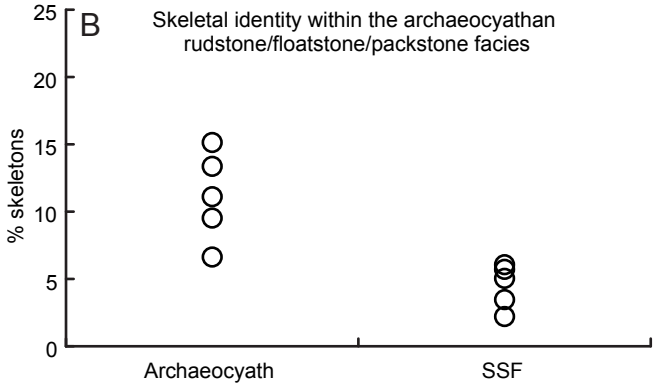
B
Skeletal identity within the archaeocyathan rudstone/floatstone/packstone facies
% skeletons
25
20
15
10
5
0
Archaeocyath
SSF

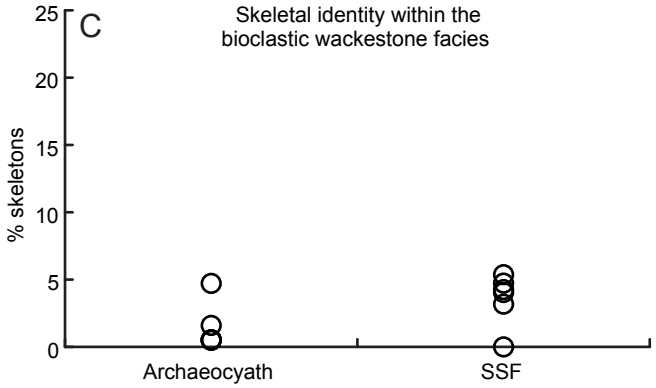
C
Skeletal identity within the bioclastic wackestone facies
% skeletons
25
20
15
10
5
0
Archaeocyath
SSF

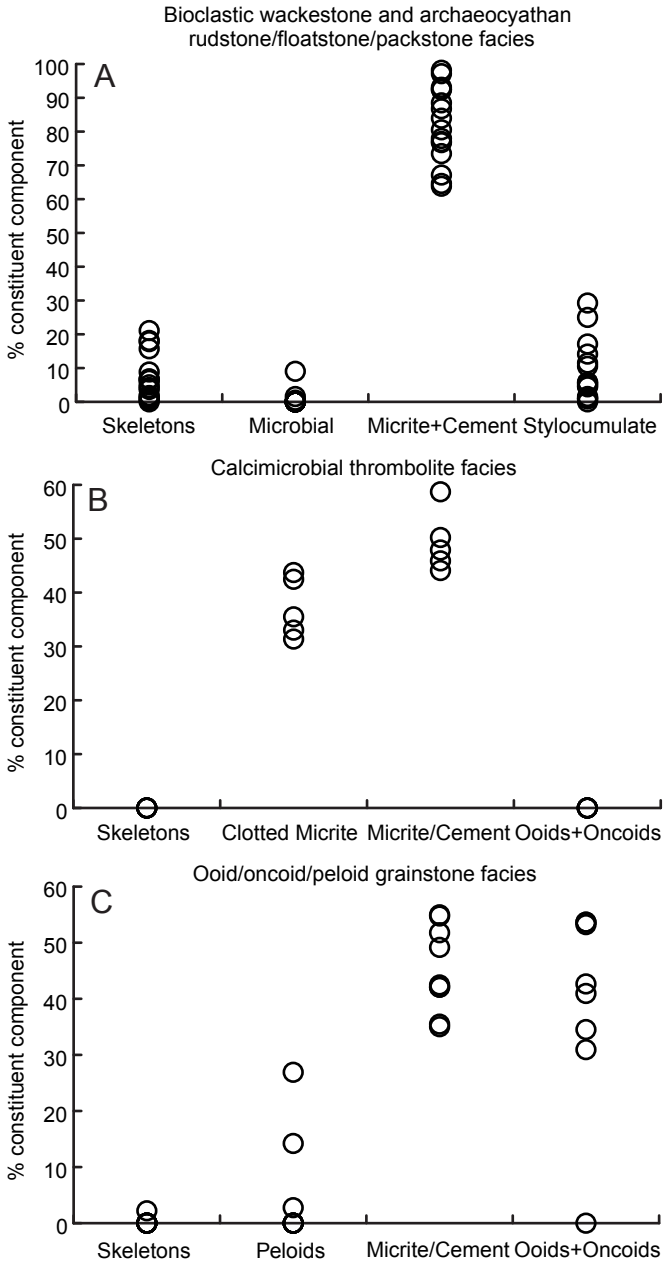
Bioclastic wackestone and archaeocyathan rudstone/floatstone/packstone facies
A
% constituent component
100
90
80
70
60
50
40
30
20
10
0
Skeletons
Microbial
Micrite+Cement
Stylocumulate
Calcimicrobial thrombolite facies
B
% constituent component
60
50
40
30
20
10
0
Skeletons
Clotted Micrite
Micrite/Cement
Ooids+Oncoids
Ooid/oncoid/peloid grainstone facies
C
% constituent component
60
50
40
30
20
10
0
Skeletons
Peloids
Micrite/Cement
Ooids+Oncoids

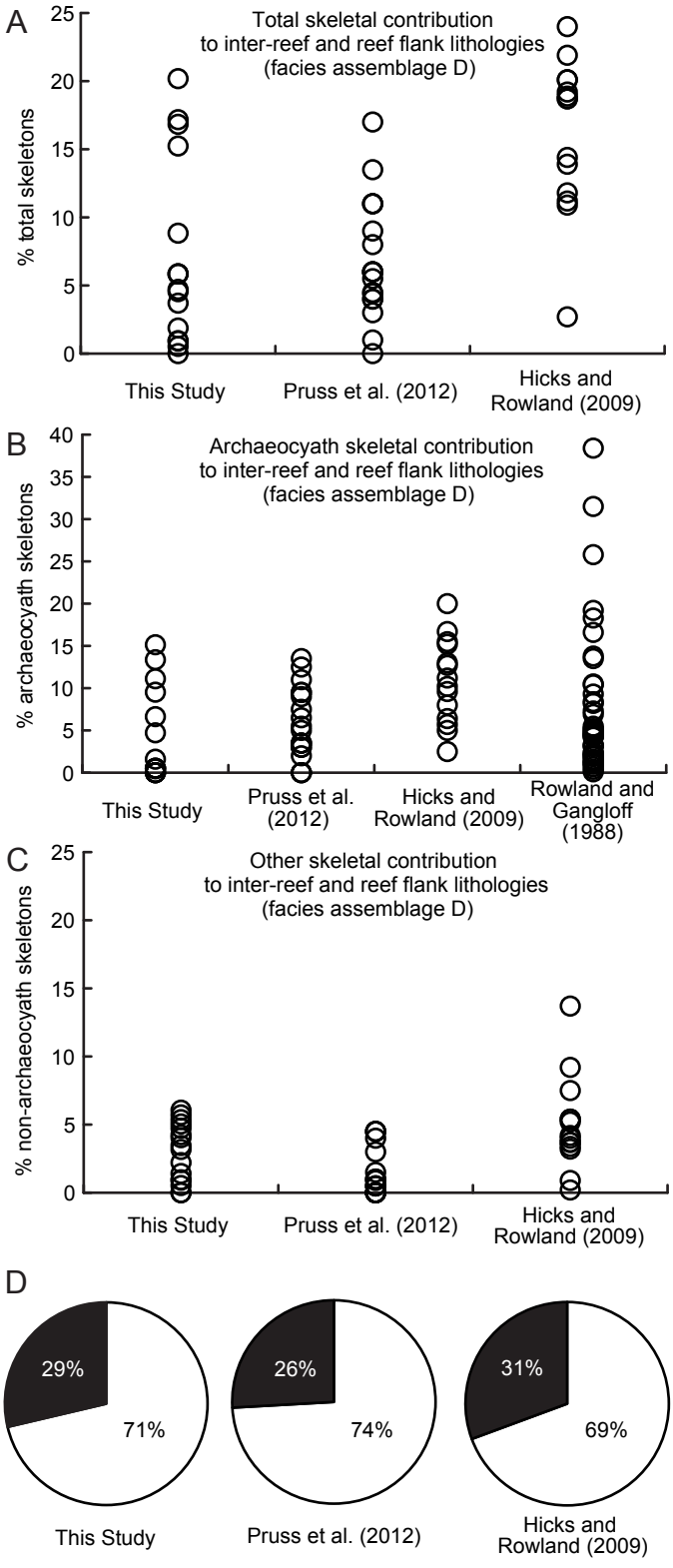
A
Total skeletal contribution
to inter-reef and reef flank lithologies
(facies assemblage D)
% total skeletons
25
20
15
10
5
0
This Study
Pruss et al. (2012)
Hicks and
Rowland (2009)
B
Archaeocyath skeletal contribution
to inter-reef and reef flank lithologies
(facies assemblage D)
% archaeocyath skeletons
40
35
30
25
20
15
10
5
0
This Study
Pruss et al.
(2012)
Hicks and
Rowland (2009)
Rowland and
Gangloff
(1988)
C
Other skeletal contribution
to inter-reef and reef flank lithologies
(facies assemblage D)
% non-archaeocyath skeletons
25
20
15
10
5
0
This Study
Pruss et al. (2012)
Hicks and
Rowland (2009)
D
29%
71%
This Study
26%
74%
Pruss et al. (2012)
31%
69%
Hicks and
Rowland (2009)